

PSFC/RR-97-1

DOE/ET-51013-322

**Capture, Storage, and Analysis of Video
Images on the Alcator C-Mod Tokamak**

A.J. Allen

February 1997

This work was supported by the U. S. Department of Energy Contract No. DE-AC02-78ET51013. Reproduction, translation, publication, use and disposal, in whole or in part by or for the United States government is permitted.

Capture, Storage, and Analysis of Video Images on the Alcator C-Mod Tokamak

by

Aaron John Allen

B.S.E., Nuclear Engineering (1994)
University of Michigan, Ann Arbor

Submitted to the Department of Nuclear Engineering
in partial fulfillment of the requirements for the degree of

Master of Science

at the

MASSACHUSETTS INSTITUTE OF TECHNOLOGY

February 1997

© 1997 Massachusetts Institute of Technology. All rights reserved.

Author

Department of Nuclear Engineering
January 29, 1997

Certified by

James L. Terry
Research Scientist, PSFC
Thesis Supervisor

Certified by

Ian H. Hutchinson
Professor of Nuclear Engineering
Thesis Supervisor

Accepted by

Jeffrey P. Freidberg, Professor of Nuclear Engineering
Chairman, Departmental Committee on Graduate Students

Capture, Storage, and Analysis of Video Images on the Alcator C-Mod Tokamak

by

Aaron John Allen

Submitted to the Department of Nuclear Engineering
on January 29, 1997, in partial fulfillment of the
requirements for the degree of
Master of Science

Abstract

Currently, Alcator C-Mod utilizes up to five arrays of filtered, visible light detectors [1] to tomographically reconstruct the D_α emission from D_α brightness data [2]. These consist of ~ 250 chords and require determination of the view of each detector, as well as an absolute intensity calibration of the view of each array. With the introduction of filtered TV cameras with CCD detectors on Alcator C-Mod, however, a view with over 300,000 different chords is available from a single camera. Since there is only one detector array, only one calibration must be made. Using a wide angle lens, large emission regions can be observed, and if toroidal symmetry is assumed, these multichord images may be inverted to yield 2D poloidal cross sections of emission power density. The use of CCD images required solution of new problems. The large amount of data available, put great demands on the current data handling, storage, and manipulation technology. This thesis describes the video system which has been implemented on Alcator C-Mod to digitize, store, and retrieve camera data. It also describes the development of a reliable, efficient, and quick procedure for inverting video images to get 2D poloidal emission power density information.

Thesis Supervisor: James L. Terry

Title: Research Scientist, PSFC

Thesis Supervisor: Ian H. Hutchinson

Title: Professor of Nuclear Engineering

Acknowledgments

I would like to thank the entire Spectroscopy group for their assistance and humor (Rice, Cheese Boy, Hana, Lo-Boy, etc.) It has been an enjoyable two years! I would like to thank my advisor Jim Terry for always seeing past my blunders and putting me on the right track again. I would like to give a big thanks to Ian Hutchinson for keeping me on the straight-and-narrow, and for giving me numerous suggestions that greatly improved this thesis. I must also acknowledge all the work done by Josh Stillerman in the writing of the new framegrabbing software. Finally, most of all, I would like to thank my family for all the love and support that they have given me over the years. I couldn't have done it without you.

Contents

1	Background	13
1.1	The Importance of Plasma Edge Research	13
1.2	The Role of Alcator C-Mod in Plasma Fusion Research	14
1.3	Diagnostics on Alcator C-Mod Used to Study the Plasma Edge	16
1.4	Goals of This Thesis and Outline	17
2	Capture, Storage, and Retrieval of Video Frames	19
2.1	Challenges of Video Capture, Storage, and Retrieval on C-Mod	19
2.2	Specifics of the Capture and Storage Hardware and Procedures	20
2.3	Data Compression of C-Mod Video Frames	22
3	Preliminaries of the Inversion Procedure	25
3.1	The Mathematics of Frame Inversion	25
3.2	Preliminary Assumptions	27
3.3	Determination of the Viewing Geometry	30
3.4	Determination of the Sensitivity of the CCD Array	35
3.5	Inversion Equations for the Wide Angle View on Alcator C-Mod	41
4	Solution of the Inversion Problem and Results	45
4.1	Solution of the Inversion Problem	46
4.2	Verification of the Inversion Method	49
4.3	Optimization of the w_{ij} Cutoff for Inversion of Video Frames	53

4.4	The Effect of 5:1 JPEG Compression on Inversion Results	66
5	More Results, Summary, and Future Work	69
5.1	More Inversion Results	69
5.2	Summary	80
5.3	Future Work	83
A	Steps Required to Invert Video Frames to Get Corresponding Emis- sion Power Density Profiles	85

List of Figures

1-1	Cross-Section of the Alcator C-Mod Tokamak	15
1-2	Alcator C-Mod Tokamak Vacuum Vessel Cross-Section	16
2-1	Schematic of the Alcator C-Mod Video Capture, Storage, and Retrieval System	21
2-2	The Video Capture and Storage Procedure	22
2-3	Percentage of Total Frame Pixels with a Given Pixel Value Error vs. Pixel Value Error for a Typical 5:1 JPEG Compressed Video Frame Viewing the Plasma	23
2-4	Average Pixel Value Error vs. Pixel Value for a Typical 5:1 JPEG Compressed Video Frame Viewing the Plasma	24
2-5	Average Pixel Value Error vs. Pixel Value Gradient for a Typical 5:1 JPEG Compressed Video Frame Viewing the Plasma	24
3-1	A Typical Alcator C-Mod Video Frame	26
3-2	Typical C-Mod Frame Used for the Toroidal Symmetry Comparison	27
3-3	The Degree of Toroidal Symmetry in a Typical C-Mod Video Frame	28
3-4	A “Thin” Frame Pixel Chord	29
3-5	A “Finite” Frame Pixel Chord	29
3-6	Preservation of Angle Between Object and Image Space in the Absence of Aberrations	30
3-7	Some Parameters Needed to Determine the Camera View	31

3-8	The Effect of Barrel Image Distortion on a Square Grid	32
3-9	The Effect of Barrel Image Distortion on a Captured Frame	32
3-10	Modelled Angle Corrections for Barrel Distortion in Captured Frames	33
3-11	Rendered Known and Seen Objects on a C-Mod Video Frame	34
3-12	The Transmission Function of the Colored Glass Filters	36
3-13	The Labsphere Calibration Frame	36
3-14	Surface Plot of the Labsphere Calibration Frame	38
3-15	Surface Plot of the Labsphere Calibration Frame After Applying the Factor 'F'	38
3-16	One of the Hydrogen Lamp Frames Used to Test the D_α Filter for Angle Dependence	40
3-17	The 32x42 Emission Mesh Chosen for the Inversion	41
3-18	The 132x251 Video Frame Section Chosen for the Inversion	42
3-19	The Path of a Frame Pixel Chord Viewing the Top of the Nose of the Tokamak Central Column	44
3-20	Number of Frame Pixel Chords Crossing a Given Emission Mesh Cell	44
4-1	The Diagonals, w_{ij} , of the 'W' Matrix	48
4-2	Checkerboard Test Emission Profile Used to Test the Video Frame Inversion Procedure	51
4-3	132x251 Bitmap Projected from the Checkerboard Test Emission Profile	51
4-4	A Test Emission Profile Used to Test the Video Frame Inversion Pro- cedure	52
4-5	132x251 Bitmap Projected from the Test Emission Profile	52
4-6	Plasma Shot 960827014 at $t = 703\text{-}736\text{ms}$	54
4-7	Emission Power Density Profile for Shot 960827014 at $t = 703\text{-}736\text{ms}$ with $w_{ijmin} = 0$	54
4-8	Views of the Two Diode Arrays Used to Verify the Inversion Results .	56

4-9	Integrated Brightness Along the Chords of the Diode Array Viewing the Inner Divertor for Shot 960827014 at $t = 714\text{ms}$ with $w_{ijmin} = 0$.	57
4-10	Integrated Brightness Along the Chords of the Diode Array Viewing the Plasma From Above for Shot 960827014 at $t = 714\text{ms}$ with w_{ijmin} $= 0$	57
4-11	Emission Power Density Profile for Shot 960827014 at $t = 703\text{-}736\text{ms}$ with $w_{ijmin} = .04$	59
4-12	Reconstructed Checkerboard Test Emission Profile with $w_{ijmin} = .04$	60
4-13	Absolute Percentage Difference in the Reconstructed Checkerboard Test Emission Profile with $w_{ijmin} = .04$	61
4-14	Another Reconstructed Test Emission Profile with $w_{ijmin} = .04$. . .	61
4-15	Absolute Percentage Difference in the Reconstructed Test Emission Profile with $w_{ijmin} = .04$	62
4-16	Integrated Brightness Along the Chords of the Diode Array Viewing the Inner Divertor for Shot 960827014 at $t = 714\text{ms}$ with $w_{ijmin} = .04$	65
4-17	Integrated Brightness Along the Chords of the Diode Array Viewing the Plasma From Above for Shot 960827014 at $t = 714\text{ms}$ with $w_{ij} = .04$	65
4-18	The Inversion Results from the Uncompressed Frame from Plasma Shot 960827014 at $t = 703\text{-}736\text{ms}$	67
4-19	The Inversion Results from the 5:1 JPEG Compressed Frame from Plasma Shot 960827014 at $t = 703\text{-}736\text{ms}$	67
4-20	The Profile of The Absolute Difference Between the Inversion Results from an Uncompressed Frame vs. a 5:1 JPEG Compressed Frame for Shot 960827014 at $t = 703\text{-}736\text{ms}$	68
4-21	The Profile of The Absolute Percentage Difference Between the Inver- sion Results from an Uncompressed Frame vs. a 5:1 JPEG Compressed Frame for Shot 960827014 at $t = 703\text{-}736\text{ms}$	68
5-1	Shot 960828005 at $t = 1037\text{-}1070\text{ms}$	72

5-2	Emission Power Density Profile for Shot 960828005 at t = 1037-1070ms	73
5-3	Shot 960828005 at t = 1070-1103ms	74
5-4	Emission Power Density Profile for Shot 960828005 at t = 1070-1103ms	75
5-5	Shot 960820016 at t = 270-303ms	76
5-6	Emission Power Density Profile for Shot 960820016 at t = 270-303ms	77
5-7	Shot 960830009 at t = 837-870ms	78
5-8	Emission Power Density Profile for Shot 960830009 at t = 837-870ms	79

Chapter 1

Background

This chapter will describe briefly the importance of the plasma edge in fusion research and will explain the usefulness of emission studies in understanding plasma edge behavior. A brief overview of Alcator C-Mod's unique role in plasma and fusion research will be given, and some of the diagnostics used on C-Mod to study the plasma edge will be described. Finally, the thesis goals will be stated and an outline of its contents will be given.

1.1 The Importance of Plasma Edge Research

Prior to about 1990, fusion scientists were mainly concerned with the study of the core plasma, while the plasma edge was, for the most part, less emphasized. The plasma edge may be defined as the region between the last closed flux surface (LCFS) and any solid vessel structure (See Figure 1-2 for orientation). The emphasis on the core plasma is understandable since all fusion reactions occur there. As it turns out, however, the plasma edge can influence strongly the behavior of the central plasma. Transport can be greatly influenced by edge conditions. Therefore, it is likely that the physics at the edge must be understood before magnetic fusion can be used as a viable energy source [3].

One of the diagnostic tools that can be used to study the plasma edge is examination of the shape and behavior of emission regions [4]. Plasmas mainly emit radiation in the soft x-ray and vacuum ultra-violet spectral regimes, but near material surfaces, the temperature is cool enough for the plasma to emit strongly in the visible. This allows analysis using simple diode detectors and CCD arrays. Using filtered views, it is possible to determine the intensity and structure of various line emitters present in the plasma. This information can then be used to study edge phenomena such as impurity recycling [5], plasma detachment [6], and MARFE's^a [7, 8]

1.2 The Role of Alcator C-Mod in Plasma Fusion Research

The Alcator C-Mod tokamak has a unique role to play in world fusion research. C-Mod is the third in a series of tokamaks (Alcator A, Alcator C) at MIT, and is a continuation of the philosophy begun at MIT in the late 1970's [9] of building high performance, high field tokamaks which are compact in size (in comparison with other tokamaks around the world), but still allow investigation of plasma regimes obtained by much larger machines. This compactness results in lower operating costs, which has allowed Alcator C-Mod to remain competitive in a time when there are much tighter budgets in the scientific community.

Figure 1-1 shows a cross-section of the Alcator C-Mod Tokamak [10]. The toroidal field is created by 10 individual liquid nitrogen cooled copper magnets (TF magnets) that allow a field of up to 9 Tesla on axis. Liquid nitrogen cooling allows the copper to have nearly six times the conductivity of copper at room temperature. The central ohmic coil (OH coil) is designed to produce up to 3 MA of inductive current in the plasma with 7.5 Wb of flux swing. Plasma shaping is accomplished by 5 pairs of poloidal field coils (EF coils). The plasma column is D-shaped in cross-section (See

^aMultifaceted Asymmetric Radiation From the Edge

Figure 1-2) and is generally diverted in the lower divertor (closed divertor), although limiter or upper divertor (open divertor) operation is possible. The entire system is powered by a 75 ton flywheel that can store nearly 2000 MJ of energy.

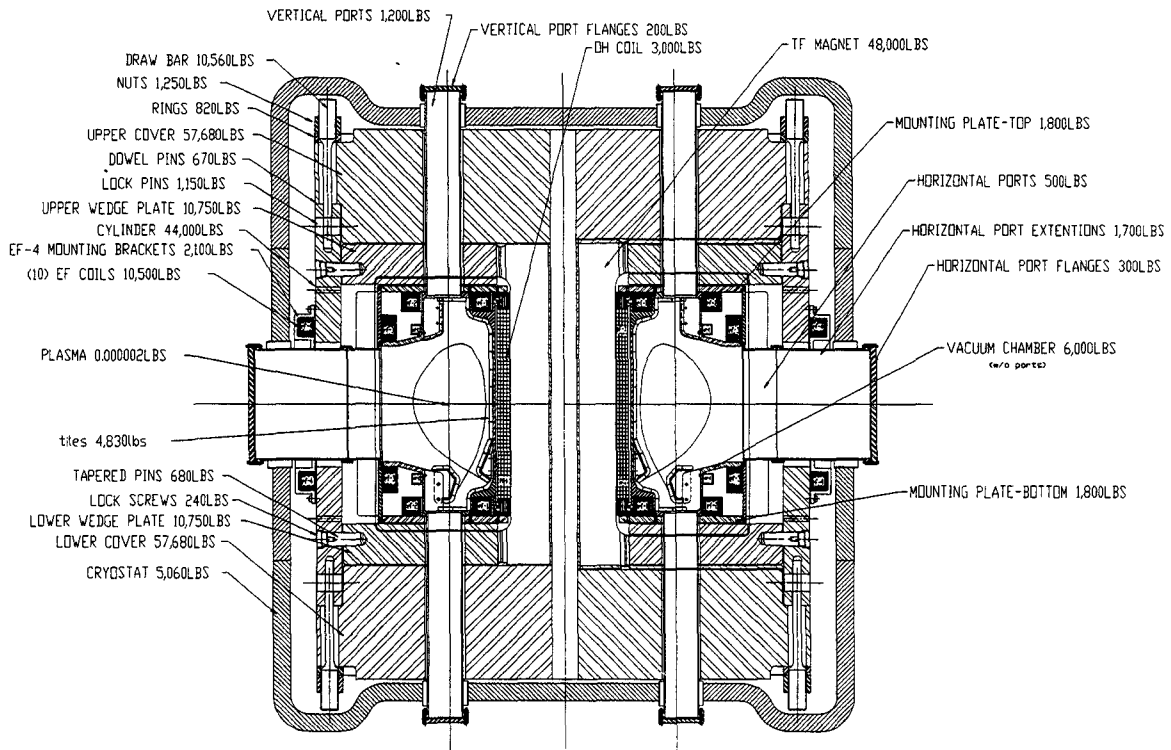


Figure 1-1: Cross-Section of the Alcator C-Mod Tokamak

The tokamak vacuum vessel is forged from stainless steel and the plasma facing components are covered with nearly 7000 molybdenum tiles. Molybdenum was chosen for its high melting temperature and heat conductivity, and has given the fusion community a good look at the costs and benefits of using high Z materials to absorb the plasma heat load. Recently, C-Mod began coating the tiles with boron and this has greatly reduced the level of molybdenum in the plasma and has nearly doubled the confinement time by improving the quality of H-mode confinement [11]. In addition, boronization allowed the desirable molybdenum characteristics to remain since the boron coating is thin.

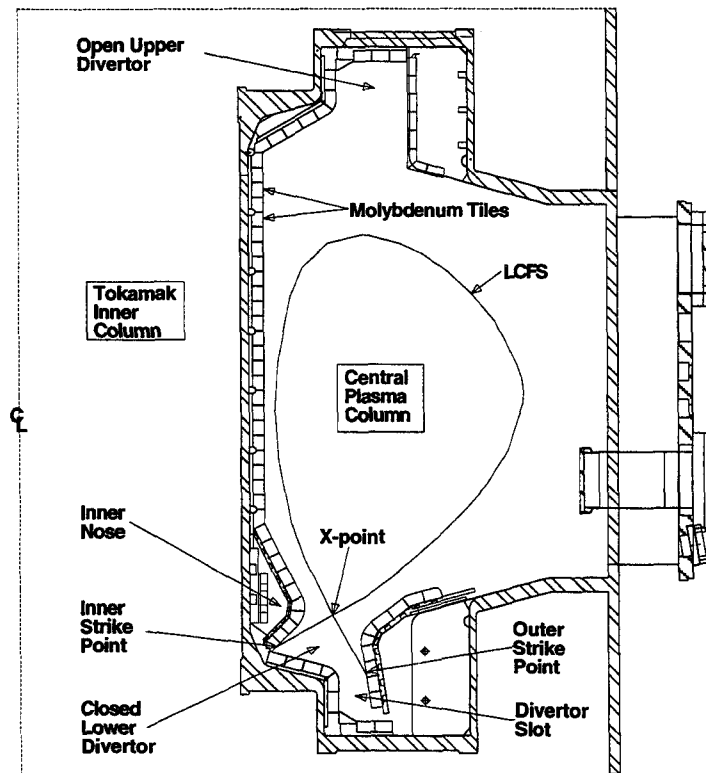


Figure 1-2: Alcator C-Mod Tokamak Vacuum Vessel Cross-Section

1.3 Diagnostics on Alcator C-Mod Used to Study the Plasma Edge

There are a great number of plasma edge diagnostics on Alcator C-Mod. A brief list of the most important will be given here along with their functions.

2π Bolometer: A diode that views the main plasma and measures approximately its total radiated power [12].

Visible Diode Array System: Various diode array views used to measure visible light in the plasma and divertor with good spatial resolution. The information from these views is used to tomographically reconstruct D_α emission power density profiles (volumetric emissivity) [2].

Thermocouples: Used to measure the bulk temperature of the molybdenum plasma

facing tiles in the tokamak.

Langmuir Probes: Probes found at numerous places around the tokamak on inner and outer divertor plates. Used to measure electron density and temperature (n_e and T_e) locally.

Fast Scanning Probe: Four independent, pneumatically driven Langmuir probes on a single head that allow measurement of the upstream (from the outer divertor plate) n_e and T_e . Scans across the scrape-off-layer (SOL) in ~ 100 ms [13].

Gas Puffing System: A gas injection system that can introduce impurities into the SOL at various points around the tokamak (e.g. divertor, midplane) to study flows in the SOL and impurity transport into the plasma core [14].

Reflectometry: Waves reflected off critical density layers in the plasma to measure electron density fluctuations (\tilde{n}_e) at the plasma edge [15].

Neutral Pressure Gauges: Pressure gauges that measure the neutral background pressure at the midplane and in the divertor [16].

CCD Camera Video: Imaging system using CCD cameras that captures video of visible emission from any one of several views of the plasma [17]. A wide angle view filtered for D_α emission is being used to “invert” brightness information from captured video frames to get emission power density profiles. This diagnostic is the subject of this thesis.

1.4 Goals of This Thesis and Outline

This thesis describes the video capture, storage, and retrieval system on the Alcator C-Mod tokamak. This system captures video from any one of several CCD cameras that view the plasma from various locations around the tokamak. The thesis will also describe the development and the results of an “inversion” routine, for one of the CCD camera views, that is being used to reconstruct emission power density values

in the scrape-off-layer (SOL) and divertor region of the plasma from brightness data (D_α emission in this case) in captured frames.

Chapter 2 will describe in detail the capture, storage, and retrieval system for video of plasma discharges.

Chapter 3 will explain the preliminary work necessary to allow the calculation of plasma emission power density profiles from video frame brightness data (“frame inversion”).

Chapter 4 will describe the procedures used in solving the frame inversion problem for a wide angle view of the plasma and will give inversion results for a video frame from that view.

Chapter 5 will give more inversion results, a summary of the thesis, and will speculate on the future paths that may be taken to improve the inversion procedure.

Chapter 2

Capture, Storage, and Retrieval of Video Frames

This chapter will describe the equipment and procedures necessary to routinely capture, store, and retrieve the large amounts of video information from Alcator C-Mod plasma discharges.

2.1 Challenges of Video Capture, Storage, and Retrieval on C-Mod

The challenges of capturing, storing, and retrieving video frames are numerous. A framegrabber board captures video from a given camera at 30 frames per second (fps) for the 1.5 seconds of a typical plasma discharge. Given 640x480 pixel resolution for each frame ($\sim 300,000$ pixels), each discharge results in about 15 MB of information. Over a typical day of about 30 plasma “shots” (discharges), 450 MB of data are taken. The difficulties involved here are digitally capturing this information in “real-time” and storing this information on an inexpensive and easily accessible external medium for later analysis. An external medium is necessary, because the amount of data involved will fill relatively expensive hard drive space in a short period of

time. Also, any capture and storage system must be automated so that the user need not be present to initiate the capture cycle. To have an absolute time reference, the capture procedure must be started with an external trigger supplied by the same time sequencing system that initiates the plasma discharge. A stop trigger is also useful in the event of an unexpected end of a discharge (e.g. a plasma disruption) where it would not be necessary to capture the subsequent dark frames.

2.2 Specifics of the Capture and Storage Hardware and Procedures

As shown in Figure 2-1, the video system has four basic components: (1) video cameras, (2) a framegrabber board for capturing and routing video, (3) a PC^a that temporarily stores video frames, and (4) a CD-write/read device for permanent data storage^b. The cameras are 8-bit RS-170 cameras that take video at 30 fps with 640x480 resolution.

The video is captured from any single camera with a commercial, PC-based framegrabber board, the MuTech M-Vision 1000^c. The board's PCI bus architecture and its ability to control directly the mother board allow real-time video transfer directly into the PC's memory. This eliminates expensive framegrabber onboard memory. The number of frames that can be captured is limited only by the amount of PC RAM available. For Alcator C-Mod it is desirable to digitize at 30 fps for ~1.5 seconds, the duration of a typical C-Mod discharge. Thus, the PC is equipped with 32 MB of RAM, which is sufficient for the ~15 MB of video as well as the overhead needed for running the Windows applications. The video is captured reliably in real-time at 30 fps with known synchronization, since the board has an external "on" gate. When the gate goes high, the framegrabber starts capturing video. It then captures

^a120 MHz Pentium with a 1 GB hard drive and 32 MB of RAM

^bMicronet MCDPLUS/PCI

^cFramegrabber board made by the MuTech Corporation, Billerica, MA

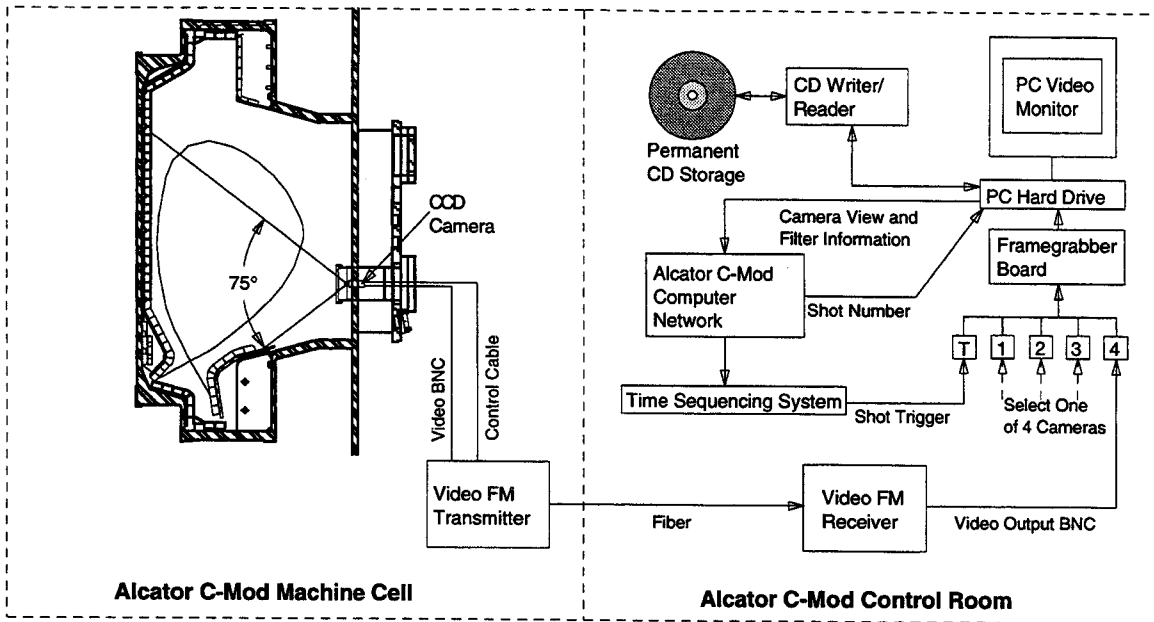


Figure 2-1: Schematic of the Alcator C-Mod Video Capture, Storage, and Retrieval System

video for 1.5 seconds (45 frames), or until the gate goes low.

If the plasma should end prematurely, a stop trigger causes the gate to go low before 1.5 seconds, and the capture procedure ends without grabbing useless frames with no plasma present. Software has been written which replays the last captured shot in a loop in slow motion after a plasma discharge^d. A fast video board was installed in order to have the capability to display the video at full speed and at full resolution.

After the capture procedure for a shot is completed, the framegrabber temporarily writes the frames to the computer hard drive. A large capacity hard drive of 1 GB was used since the video frames take up so much memory. Ultimately, the video must be permanently stored on some inexpensive and reliable, removable media since any hard drive will soon fill up. Currently, the most economical media are writable CD's with a capacity of about 650 MB per disc at a price of about \$5 each. The CD's are durable and portable which makes data retrieval relatively simple.

^dJosh Stillerman, a software engineer at the Plasma Science and Fusion Center, must be credited with writing a large portion of the framegrabbing software.

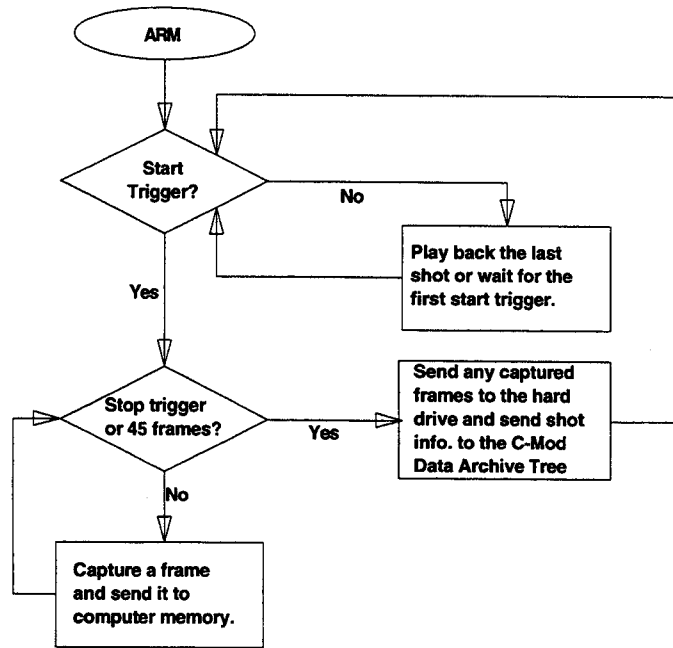


Figure 2-2: The Video Capture and Storage Procedure

2.3 Data Compression of C-Mod Video Frames

With no data compression, a CD will only hold about a day and a half's worth of video. To hold a week's worth of data (a convenient time scale) one needs about 5:1 compression. Lossless compression schemes seem to be limited to about 1.5:1 compression. Investigation of the widely used, lossy, JPEG^e compression scheme has shown that 5:1 compression is possible if one is able to accept some lost information. Typically, a 5:1 compression ratio only resulted in an average error of 1 pixel value unit (out of a full-scale value of 256), although some pixels had errors of 2-6 units, and a single pixel could have an error of as much as 20 units. Pixel value had only a minor effect on the error. However, large pixel value gradients resulted in noticeably increased error. The percentage of total frame pixels with a given error in pixel value for a typical 5:1 JPEG compressed C-Mod frame can be seen in Figure 2-3. The effects of pixel value and pixel value gradient on errors from JPEG compression can be seen in Figures 2-4 and 2-5 respectively. The effect that these losses have on inversion of

^eJoint Photographic Experts Group

a video frame will be quantified in Chapter 4. However, it should be said now that 5:1 compression leads only to small relative errors in the inversion of typical C-Mod video frames.

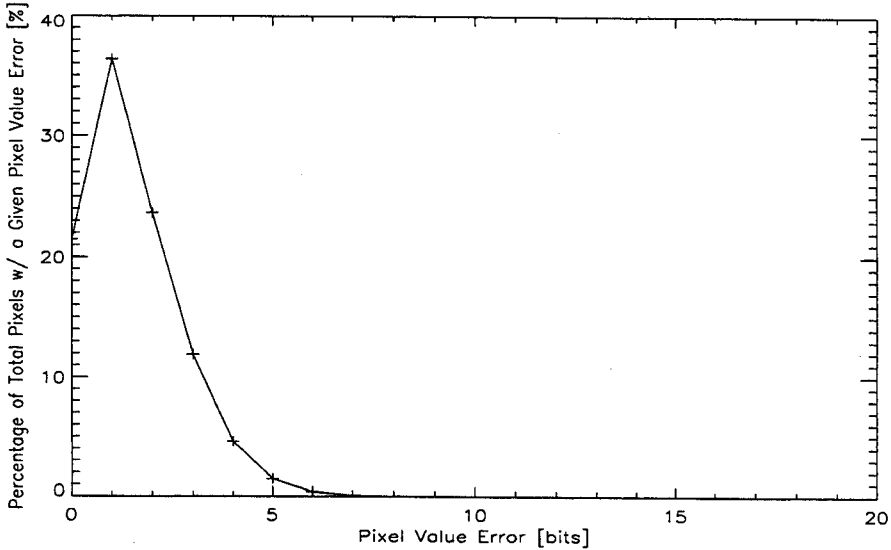


Figure 2-3: Percentage of Total Frame Pixels with a Given Pixel Value Error vs. Pixel Value Error for a Typical 5:1 JPEG Compressed Video Frame Viewing the Plasma

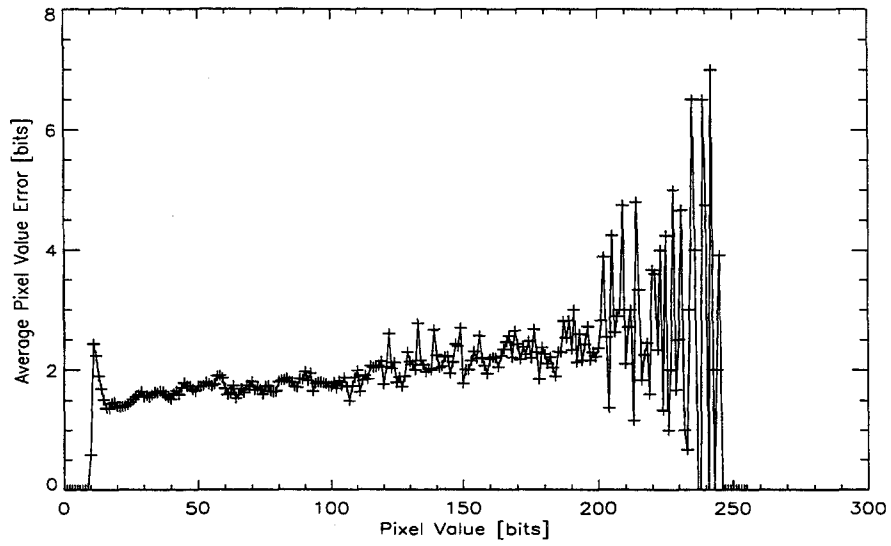


Figure 2-4: Average Pixel Value Error vs. Pixel Value for a Typical 5:1 JPEG Compressed Video Frame Viewing the Plasma

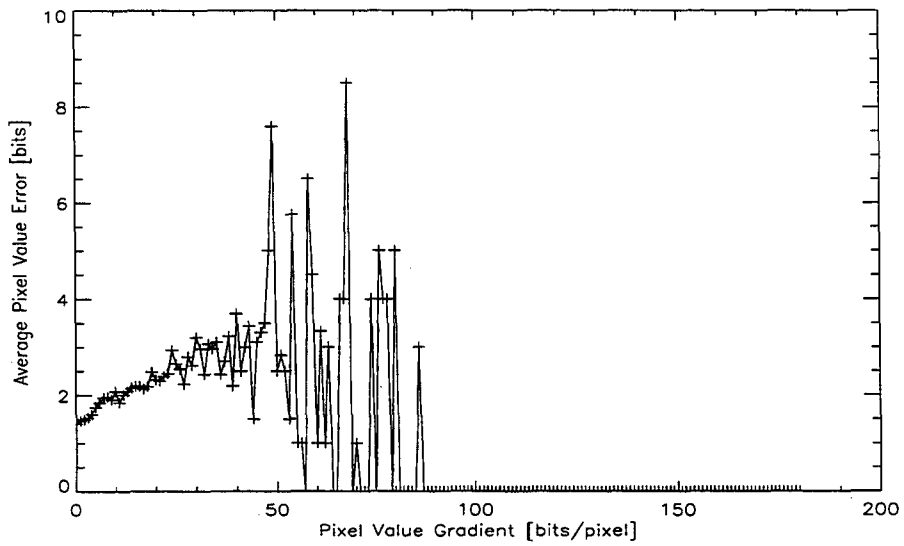


Figure 2-5: Average Pixel Value Error vs. Pixel Value Gradient for a Typical 5:1 JPEG Compressed Video Frame Viewing the Plasma

Chapter 3

Preliminaries of the Inversion Procedure

This chapter will describe the theory of calculating emission power density values from video frame brightness data. It will state two important assumptions that were made initially to make the inversion problem computationally tractable for the 640x480 video frames that are inverted in this thesis. It will describe how determination of the viewing geometry and the sensitivity of the CCD array of the camera was essential to extracting quantitative information from captured frames. Finally, it will give the specifics of the how the inversion problem was set up for a wide-angle camera view of the plasma.

3.1 The Mathematics of Frame Inversion

Inversion of video frames is a rather straightforward problem in theory. A single image (frame) is a 2D projection of individual chords through the 3D plasma environment. A typical C-Mod video frame can be seen in Figure 3-1 (For those not familiar with the environment shown, look at Figure 3-11 for some orientation.) The flux measured by an individual pixel is simply the integral of emission power density along the



Figure 3-1: A Typical Alcator C-Mod Video Frame

line-of-sight (l.o.s.). This can be seen in the equation

$$b = \frac{1}{4\pi} \int_{l.o.s.} \epsilon(l) dl \quad (3.1)$$

where, b , is the brightness the pixel sees in $[W/m^2/ster]$, ϵ , is the local plasma emission power density in $[W/m^3]$, and, dl , is the differential length along the line-of-sight in $[m]$. To solve this equation, one can discretize the emission with a chosen mesh. Then, for the pixels in a frame, one gets the vector equation

$$b_i = \frac{1}{4\pi} \sum_j (\Delta l_{ij} \epsilon_j) = \frac{1}{4\pi} \sum_j (C_{ij} \epsilon_j) \quad (3.2)$$

The elements, Δl_{ij} , are the lengths across the discrete emission cells along the line-of-sight. $C(\Delta l)$ is a 2D matrix whose dimension, i_{max} , depends on the number of frame pixels one is using and whose dimension, j_{max} , depends on the number of emission cells chosen. One must have $i_{max} \geq j_{max}$ if the problem is not to be underdetermined.

3.2 Preliminary Assumptions

Given 300,000 pixels, a simplifying assumption that the emission is toroidally symmetric has been made, at the outset, so that the inversion problem is computationally tractable [18]. This gets rid of one dimension and the plasma emission becomes a 2D entity. Analysis has shown that the toroidal symmetry assumption is typically quite good except very early and very late in the plasma discharge and during disruptions. A typical case, where the symmetry is good, can be seen in Figure 3-2. The two outlined regions on either side of the tokamak central column are compared directly in Figure 3-3 in the picture on the left. The picture on the right in Figure 3-3 shows the absolute difference between these two regions.

These two regions had an average percent difference of $\pm 13\%$. Most of the differences were concentrated in thin bands at the edges of bright emission regions, where the percent difference was as high as 100%. Some of these differences may be due to the fact that the views left and right of the tokamak central column are not exactly symmetric with respect to each other because of camera placement.

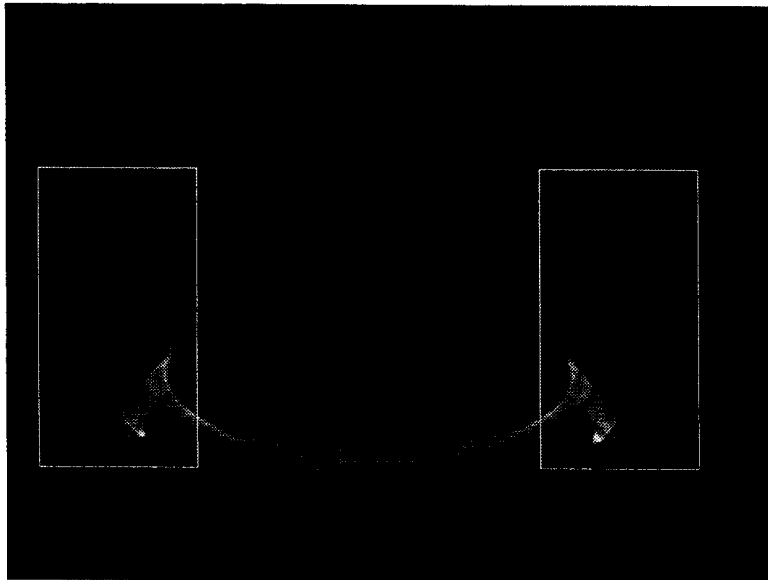


Figure 3-2: Typical C-Mod Frame Used for the Toroidal Symmetry Comparison

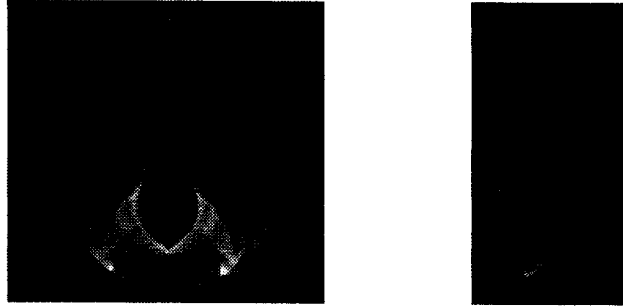


Figure 3-3: The Degree of Toroidal Symmetry in a Typical C-Mod Video Frame

Another assumption that has been made in the analysis is known as the “thin pixel” approximation [19]. Since a pixel has a finite area, its resulting projected area grows with distance from the CCD detector. At far enough distances, its area starts to become nearly as large as the chosen emission cell size. This means that up to 4 emission cells may contribute to the brightness at a given distance for C-Mod geometry. If one chooses a large enough emission cell size and if the distances that chords travel from the CCD detector are not too far, this will not be a problem. The thin pixel approximation assumes that the only emission contributing to the brightness at a given distance comes from the emission cell that contains the center point of the projected view. Figures 3-4 and 3-5 show 2D representations of the difference between a projected “thin” pixel chord and a projected “finite” pixel chord as they travel through the 3D Alcator C-Mod tokamak environment. The curving in the chords results when the chords reach a minimum major radius, R , and begin to increase in major radius.

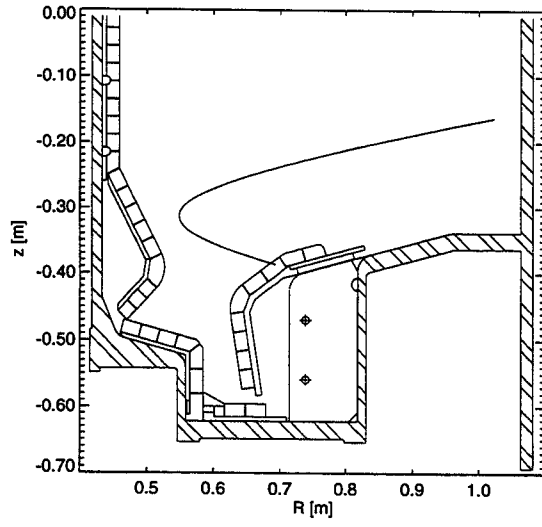


Figure 3-4: A "Thin" Frame Pixel Chord

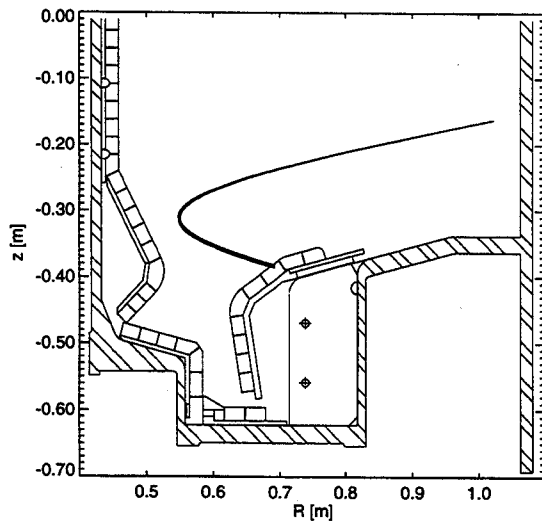


Figure 3-5: A "Finite" Frame Pixel Chord

3.3 Determination of the Viewing Geometry

In order to extract the desired quantitative information from captured video, the geometry of the view with respect to the machine geometry was determined. Once the viewing geometry was known, then viewing chords of given pixels were calculated. Knowledge of the pixel views was critical to the ultimate goal of unfolding the 2D poloidal emission power density profile from the view. In the absence of aberrations, the angle (with respect to the central ray through the lens) was preserved between object and image space (See Figure 3-6). This should allow calculation of the chordal view coordinates (relative to the plasma/vacuum vessel geometry) of any CCD pixel, given a knowledge of: the pixel array geometry, the lens focal length, the position of the lens in the vacuum vessel, and the yaw, pitch, and roll of the camera.

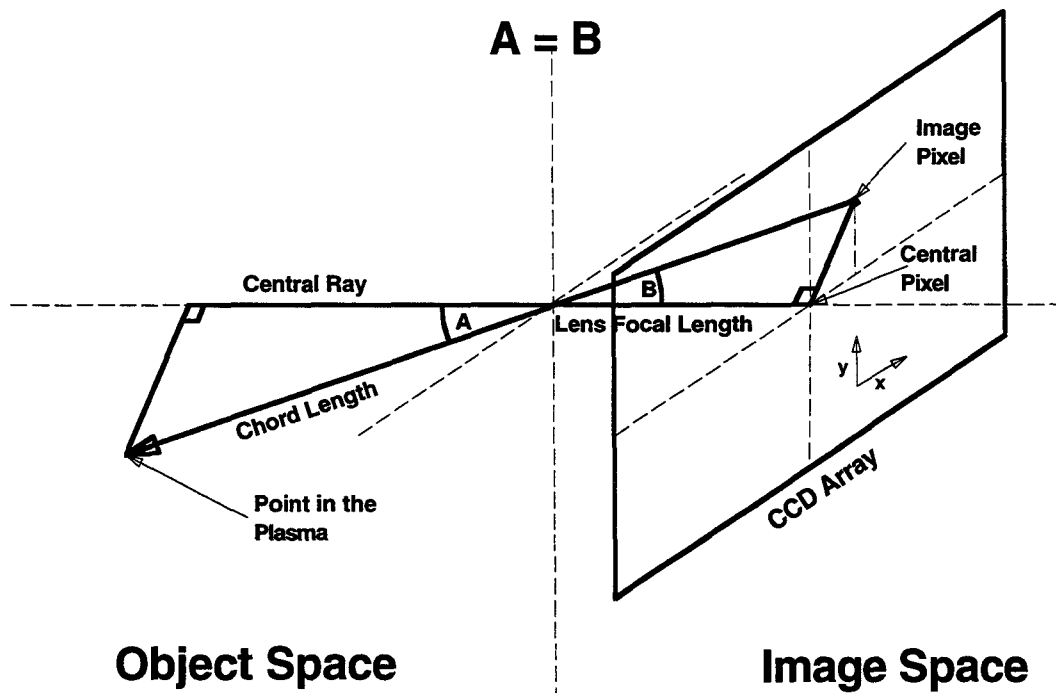


Figure 3-6: Preservation of Angle Between Object and Image Space in the Absence of Aberrations

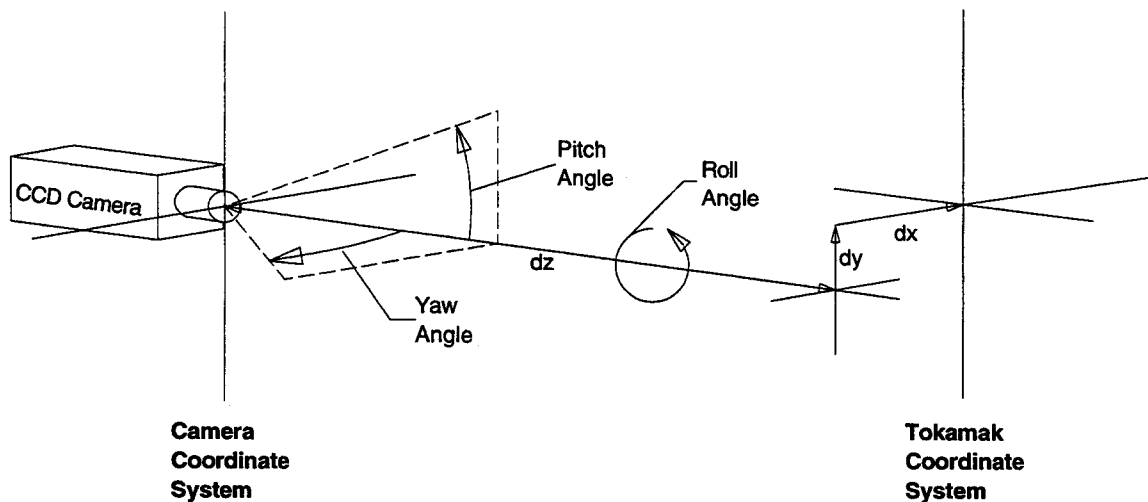
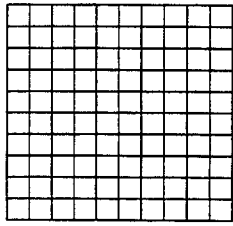


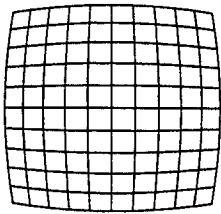
Figure 3-7: Some Parameters Needed to Determine the Camera View

In the absence of exact knowledge of all these quantities or as a check of the quantities, a calculation was made from object space to image space by using known (vessel) coordinates of objects (e.g. ports, antennas, armor tiles) to predict the pixel positions of these objects in the image. These predictions were then compared with the pixel positions that were actually observed in the image. For the wide angle view that will be used in the emission reconstruction in this thesis, significant corrections due to “barrel” image distortion [20] by the lens were required to match the predicted image positions with those measured^a. This distortion resulted from an increase in the magnification of the lens as ray angle from the central ray increased. The effect of barrel distortion on a square grid is shown in Figure 3-8. Figure 3-9 shows this effect on an actual frame captured with the video system.

^aThe lens used was a C-mount glass lens from Universe Kogaku with a nominal focal length of 4.2 mm.



Initial Square Grid



Barrel Distortion of the Square Grid

Figure 3-8: The Effect of Barrel Image Distortion on a Square Grid

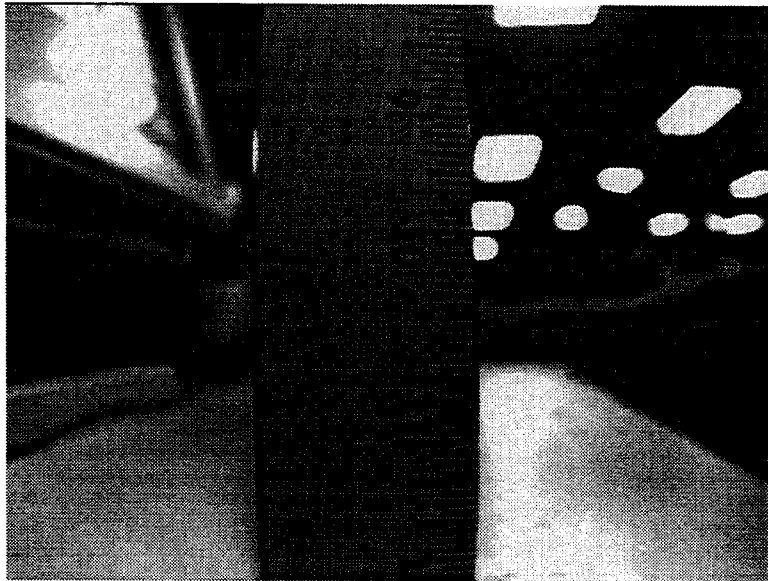


Figure 3-9: The Effect of Barrel Image Distortion on a Captured Frame

To correct for the barrel distortion present in captured frames, the angles (from the central ray of the lens) of the predicted positions of seen objects in a brightly lit frame viewing the plasma (Figure 3-11) were compared with the angles of the actual positions of these objects in the frame. Differences in the angles were then fitted versus angle to a polynomial function. It turned out that a third order function was appropriate. The fitted data used for calculating from object to image space is shown in Figure 3-10. To go from object to image space one calculates the angle from the central ray of a desired object in the tokamak, and then adds the corresponding correction factor to the angle to correct for the distortion. To go from image to object space, the factor is simply subtracted from the angle.

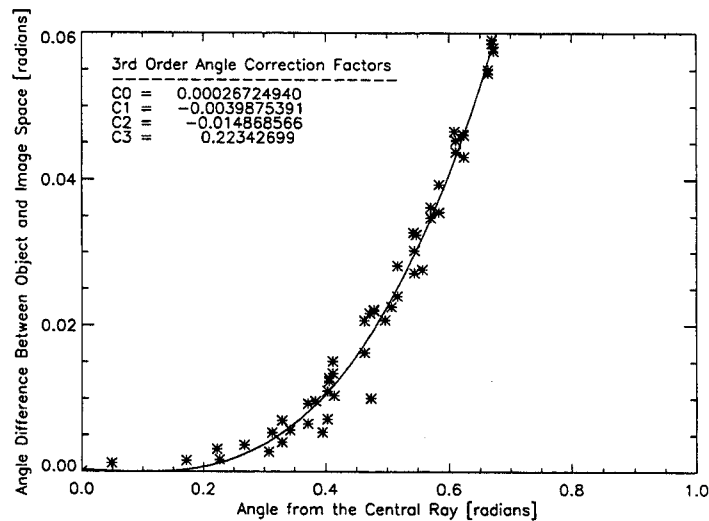


Figure 3-10: Modelled Angle Corrections for Barrel Distortion in Captured Frames

After modelling these corrections it was possible to reproduce the rendered positions of known and seen objects (e.g. the armor tiles on the inner cylinder and the location of one of the access ports). It was also possible to render magnetic surfaces, calculated by the EFIT [21] magnetic equilibrium reconstruction program, on the frames, which was useful if one wanted to know the location of magnetic surfaces with respect to visible emission regions. The results of this analysis for a brightly lit frame are shown

in Figure 3-11, showing the tokamak central column, the outer divertor region, the outer wall, the RF antenna, an access port, the location of armor tiles, and two magnetic equilibrium surfaces (See Figures 1-1 and 1-2 for machine orientation.)

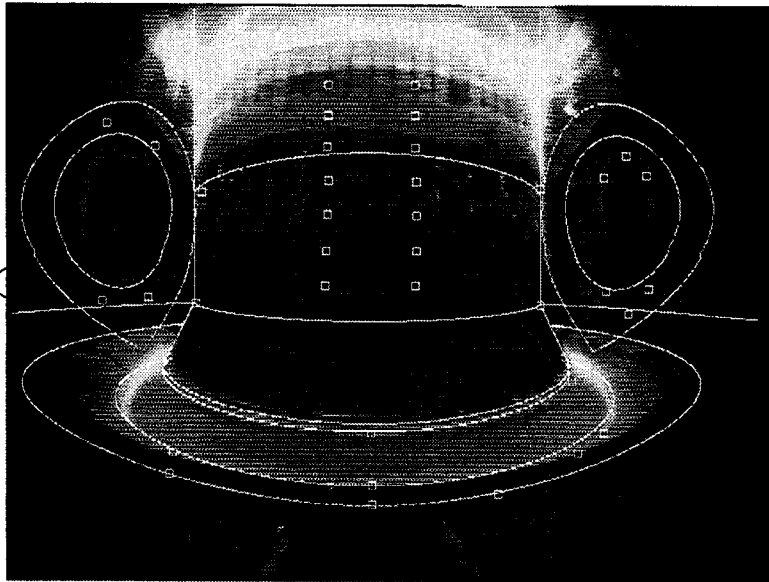


Figure 3-11: Rendered Known and Seen Objects on a C-Mod Video Frame

The equations and modelled distortion corrections were then used to follow pixel chords throughout the machine to see how individual emission cells contributed to overall brightness incident on each pixel. This was done by calculating the lengths of intersection of each pixel chord across any emission cells along the line-of-sight, given by C_{ij} (Δl_{ij}) (This is the “thin” pixel approximation at work.) Once the C_{ij} ’s were calculated, standard matrix techniques were then used to solve for ϵ_j in Equation 3.2. These matrix techniques will be explained in greater detail in Chapter 4.

3.4 Determination of the Sensitivity of the CCD Array

In order to find the pixel value resulting from an incident flux at given wavelength (i.e. calibrate pixel value with incident brightness), the sensitivity of the CCD array at that wavelength was measured. We will only be concerned with the D_α wavelength ($\lambda = 656 \text{ nm}$) in all analyses, because an D_α filter was used. The filter consisted of two colored glass filters placed face-to-face^b. One filter (red glass) was used to cut off wavelengths below 645 nm and another filter (IR) was used to cut off wavelengths above 700 nm. This is a rather wide bandpass ($\sim 55 \text{ nm}$) to measure line emission, but D_α emission is so dominant around these wavelengths that it does not matter. Standard interference filters could not be used, because some of the rays accepted by the wide angle lens were at such steep angles that the bandpass of an interference filter would be shifted significantly.

A source of known brightness (Labsphere^c) was used to calibrate the CCD array sensitivity. The Labsphere source was a continuum emission source. Since a D_α filter was being used, only brightness at wavelengths in the bandpass of the filter were relevant. Using a monochromator, the transmission function of the D_α filter was mapped out (Figure 3-12). Using the Labsphere, the total brightness under the transmission function of the D_α filter was calculated (The captured frame used in the Labsphere brightness calibration is shown in Figure 3-13.) This allowed the sensitivity of the CCD array at the D_α wavelength to be determined.

^bManufactured by Twardy Technology, Inc., Darien, CT

^cManufactured by Labsphere, Inc., North Sutton, NH

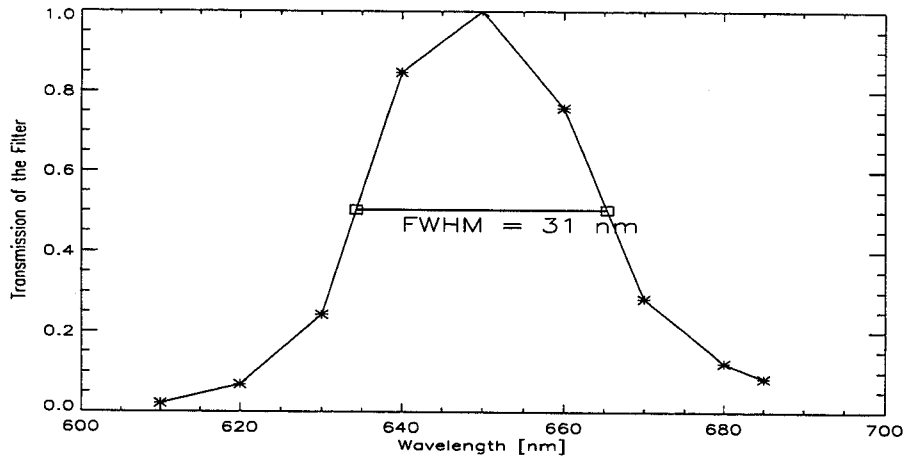


Figure 3-12: The Transmission Function of the Colored Glass Filters

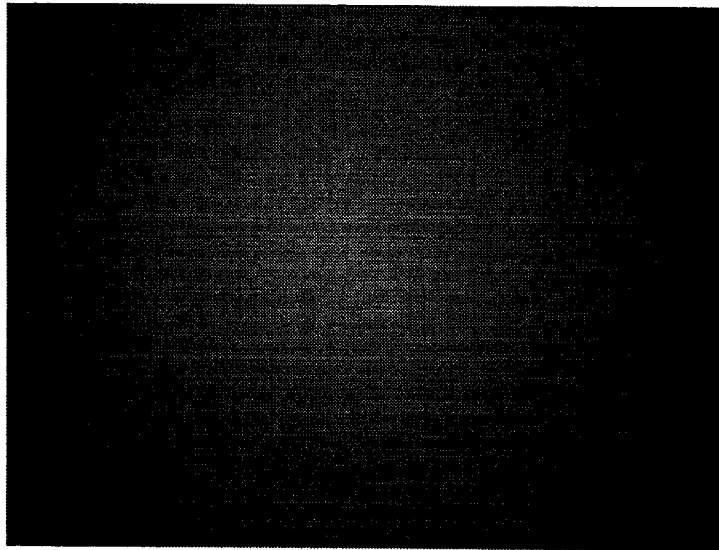


Figure 3-13: The Labsphere Calibration Frame

Figure 3-14 shows a surface plot of the pixel values of the Labsphere calibration frame in Figure 3-13 (The x and y pixel numbers have been rebinned from a 640x480 array to a 64x48 array to better facilitate the surface plotting function.) It can be seen in this figure that the pixel values fell off at a steady rate from the center of the frame. Since the Labsphere was at constant brightness, this showed that there was spatial dependence in the sensitivity of the CCD. It was not known exactly where this dependence originated from, but it was likely at least partially due to changing solid angle of the viewing pixels of the CCD array. This was because the CCD array was flat, and as a result, the solid angle subtended by a pixel changed with x and y distance from the central pixel. A convenient function, that when applied to the Labsphere frame, made the profile flat was

$$F = \left(\frac{f^2 + x^2 + y^2}{f^2} \right)^{\frac{3}{4}} \quad (3.3)$$

Where 'f' was the lens focal length in [mm] and 'x' and 'y' were the x and y distances in [mm] from the central pixel of the CCD array. The results of applying this factor to the Labsphere calibration frame can be seen in Figure 3-15. The pixel value profile was then relatively flat (within 3%), as it should be for a constant brightness source. This factor was applied to the pixel values of all captured frames used in inversions, because it allowed only one sensitivity calibration number to be used to convert pixel value to brightness.

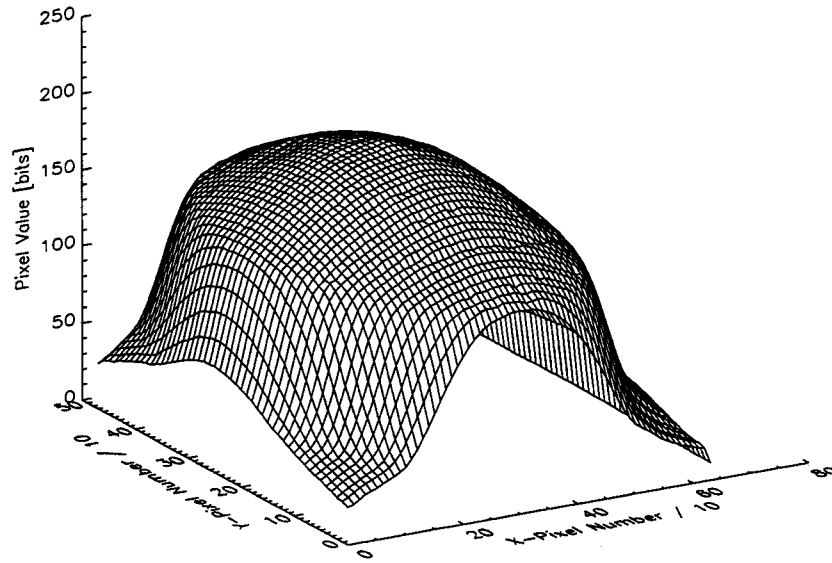


Figure 3-14: Surface Plot of the Labsphere Calibration Frame

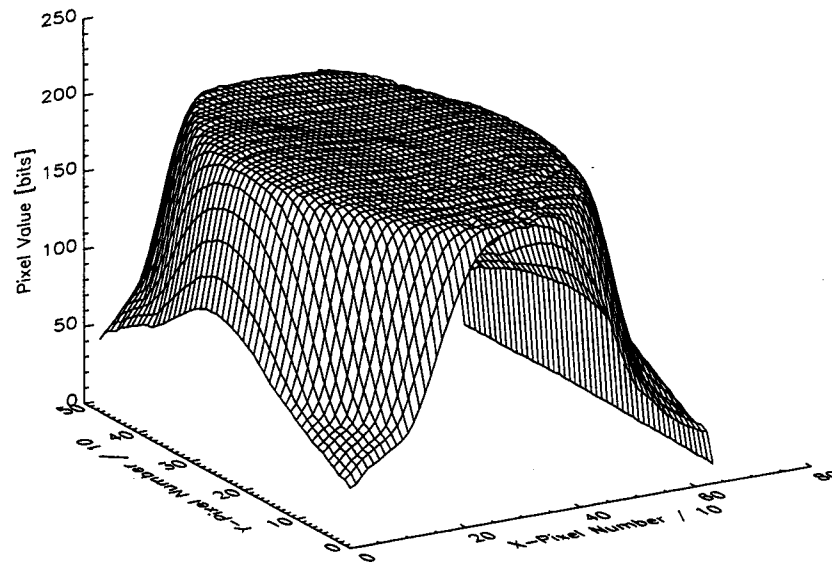


Figure 3-15: Surface Plot of the Labsphere Calibration Frame After Applying the Factor 'F'

Another concern of the CCD array calibration was that the bandpass of the D_α filter might have some angular dependence, since the Labsphere calibration utilized a continuum source, while in the experiment, a single line (D_α) within the bandpass was measured. The Labsphere calibration was a necessary but insufficient test to show that there was little or no angular dependence of the bandpass of the filter, because the shape of the filter transmission function could change, while the area underneath it remained constant.

To test this, frames viewing a hydrogen lamp (line source) were captured (e.g. Figure 3-16), with the lamp located at various places in the frame. Since the lamp was AC, a number of frames were taken for each position and averaged. An upper limit on the effect of angular dependence of the filter was found to be $\sim 2\%$ per 100 pixels from the central pixel (out of a maximum distance of ~ 400 pixels from the central pixel). In fact, the minimum and maximum distances (in pixels) for the section of the image that was used in the inversion (see Section 3.5) were 164 and 318. Thus, the maximum error in the relative brightness calibration for D_α emission, due the use of a continuum source, was about 6%. Another simple test that was done was to measure the total signal with a voltmeter from a diode detector filtered with the glass filters and illuminated with an incandescent light bulb. The filters were then tilted at an arbitrary angle ($\sim 45^\circ$) which changed the the angle of incidence of the viewing chords to the filter and the signal was measured again. It was found that the total difference between these two signals was about 8%.

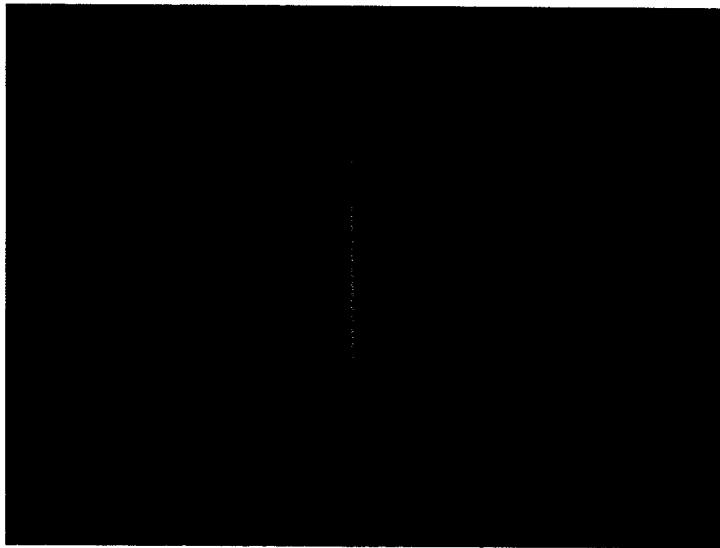


Figure 3-16: One of the Hydrogen Lamp Frames Used to Test the D_α Filter for Angle Dependence

3.5 Inversion Equations for the Wide Angle View on Alcator C-Mod

For the analysis of the wide angle view, an emission mesh was chosen, and an array of pixels that viewed this region was defined. An emission mesh of 32x42 cells was chosen around the divertor region which gave (1cm x 1cm) resolution, and is shown in Figure 3-17. It was found that a 132x251 section out of the total 640x480 frame covered this region well. This 132x251 section, along with its corresponding 640x480 frame, is shown in Figure 3-18.

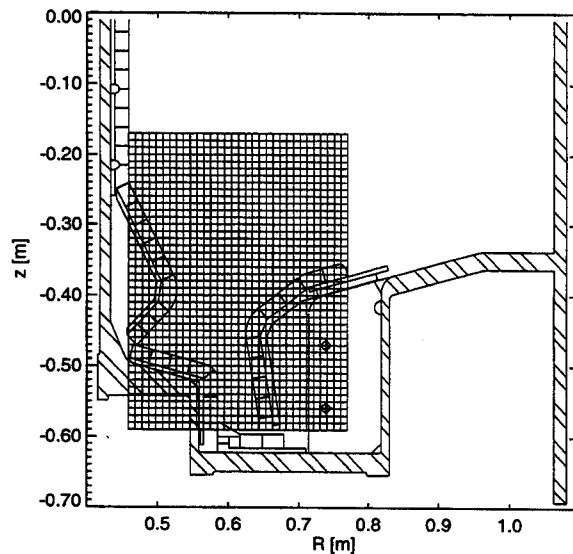


Figure 3-17: The 32x42 Emission Mesh Chosen for the Inversion

The emission mesh and the bitmap section were used to calculate the $C (\Delta I)$ matrix. To test the algorithm used to calculate C , the chords from pixels viewing known objects in a frame were followed to see if they traveled to the R and z locations of the objects. Figure 3-19 shows the path of a chord that viewed the top of the nose (see Figure 1-2 for machine orientation) on the right side of the tokamak central column in the view. This chord passes near this point in the figure, and just clears the column to continue on further. This process was done for a number of seen objects in the

frame, and the results showed that the C matrix could be calculated accurately.

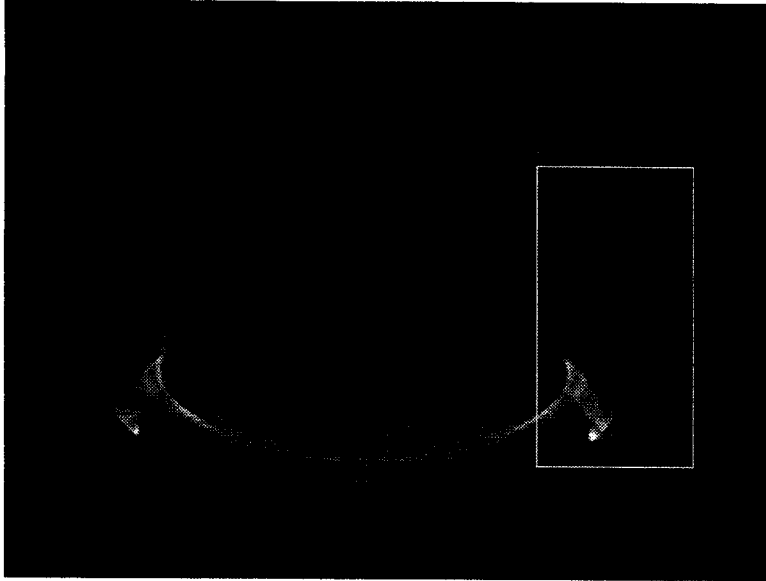


Figure 3-18: The 132x251 Video Frame Section Chosen for the Inversion

The calculation of the C matrix for the 132x251 frame section required about five hours of VAX Alpha workstation time and resulted in a very large matrix ($33132 \times 1344 = 4.453 \times 10^7$ elements). This matrix was quite sparse ($\sim 2\%$ populated), however, and only 19317×811 of the total elements were nonzero since some pixels had no intersections and some emission cells were inside of tokamak components (The cells inside of the machine components were only used to give the emission grid a rectangular shape.) The matrix's sparseness allowed storage in a compressed form which amounted to about 7 MB worth of information.

Figure 3-20 shows the number of pixel chords that crossed a given emission cell in 'C'. The frequency of the crossings showed that the problem was quite overdetermined for most of the emission cells, although the number of crossings was as low as 7 for some cells in the divertor "slot". One possible way to reduce the size of C would be to selectively throw out many of the redundant pixels while still keeping acceptable accuracy. As will be shown in Chapter 4, the inversion procedure for the C matrix

in this analysis is fast enough that no values need to be thrown out. However, this may not be the case if one wishes to increase the range of the emission mesh in the future (By doubling the number of emission cells, one needs to approximately double the number of frame pixels, which makes the problem four times larger.)

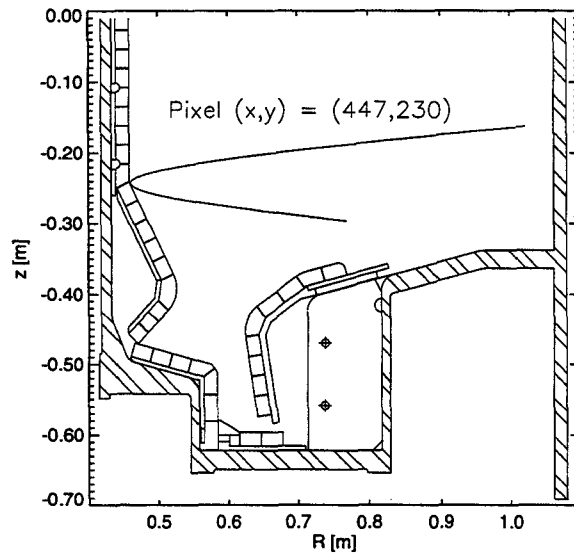


Figure 3-19: The Path of a Frame Pixel Chord Viewing the Top of the Nose of the Tokamak Central Column

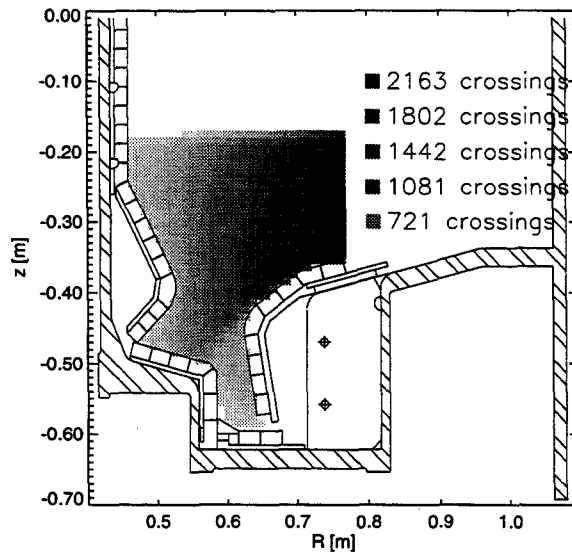


Figure 3-20: Number of Frame Pixel Chords Crossing a Given Emission Mesh Cell

Chapter 4

Solution of the Inversion Problem and Results

This chapter will describe the method used to solve the discretized brightness equations for emission power density in the wide angle view on Alcator C-Mod. It will be explained why it was necessary to apply a singular value decomposition (SVD) when solving the equations because of an ill-conditioned matrix. It will be shown how the inversion solution was tested using known “test” emission profiles. The results of an inversion of a video frame viewing a plasma discharge will then be presented and it will be shown why more stringent conditions (more smoothing) were needed in the SVD to get believable solutions for real frames than were required for the test emission frames (the condition number of $C^T C$ had to be reduced). It will be shown how other diagnostics that measure D_α emission were instrumental in determining what the optimum condition number was to keep smoothing at a minimum while getting reasonable results for inversions of real video frames. Finally, the effect of 5:1 JPEG compression on inversion results will be presented.

4.1 Solution of the Inversion Problem

Once each C_{ij} was known from the geometry, then the vector equation

$$b_i = \frac{1}{4\pi} \sum_j C_{ij} \epsilon_j \quad (4.1)$$

was solved to get the desired emission power densities, ϵ_j . There are a number of ways to do this. One method is to solve a least squares minimization problem where one tries to minimize the error

$$\epsilon = \left(\frac{1}{4\pi} C \epsilon - b \right) \quad (4.2)$$

This process was used by Fenstermacher, et al. at LLNL with success for a problem of similar size [22]. Unfortunately, the process took over two weeks of distributed workstation time, and is unacceptable if one wants to find the emission power densities of frames routinely.

Another way to calculate the power densities is to pseudo-invert the C matrix. Since the C matrix is not square, it is not possible to invert it directly. If the problem is overdetermined (more frame pixels than emission mesh cells), as it is in this case, a solution exists in the least squares sense which yields emissivity values so as to minimize the differences between the measured brightnesses and the chord integrals through the reconstructed emission. If the problem is underdetermined (more emission cells than frame pixels) a unique solution does not exist, and one must find other equations (constraints on the solution) to make the number of equations and unknowns equal.

Pseudo-inversion can be done a number of ways using packaged software, but one must be careful because, while C is sparse, its inverse will most likely not be. This was deemed unacceptable in this case because of the large amount of storage necessary

to save the full inverse (~ 60 MB). One way around this was to take the transpose of C . By multiplying the vector equation by the transpose and then solving for ϵ one got

$$\epsilon = 4\pi(C^T C)^{-1} C^T b \quad (4.3)$$

$C^T C$ is a square matrix whose size depends on how many emission cells one has. It is 811×811 in this case. The inverse of a square matrix this size can be calculated relatively quickly using packaged software. The inverted matrix, $(C^T C)^{-1}$ is not sparse, but the required storage for it is much less than the full C^{-1} matrix. The storage problem can then be handled by storing the full 811×811 $(C^T C)^{-1}$ matrix and the compressed sparse C^T matrix separately. These require a total of about 9.5 MB worth of storage which is much less than the ~ 60 MB necessary to store the full C^{-1} matrix.

One must be careful when inverting the $C^T C$ matrix, however, because it is often very poorly conditioned [23]. Poor conditioning occurs when two rows in a matrix are nearly (or exactly) degenerate, so when one row is subtracted from the other, only small values dominated by roundoff error are left. Poor conditioning can be overcome by using singular value decomposition which selects those matrix elements whose values will be dominated by roundoff error and sets them equal to zero [24]. It does not seem beneficial, at first glance, to throw out information, but the elements that make the matrix ill-conditioned tend to pull the final solution away from its correct value by a large margin. The lost information is easily overcome by getting the rest of the solution correct.

The singular value decomposition routine used to invert $C^T C$ was a double precision IMSL routine known as 'DLSVRR' [25]. Singular value decomposition converts an $N \times N$ matrix into two $N \times N$ column-orthogonal matrices, U and V , and an $N \times N$

diagonal matrix, W , whose elements are positive or zero. $C^T C$ is then given by

$$C^T C = U W V^T \quad (4.4)$$

The diagonal elements of W , which shall be called w_{ij} , determine whether the matrix is ill-conditioned or not. A number known as the condition number of the matrix, $K(C)$, quantifies this. $K(C)$ is the ratio of the largest w_{ij} element to the smallest. Ideally, a well-conditioned matrix should have $K(C) \sim 1$, but this rarely happens in real physical systems. If $K(C) = \infty$, then one or more of the w_{ij} 's is equal to 0 and the matrix, C , is singular. In the singular value decomposition algorithm, one sets a lower limit on the size of w_{ij} that is considered useful and sets to zero all lower values. The higher one sets this limit, the closer $K(C)$ gets to 1. This essentially smooths the data. One does not want to set the lower limit of acceptable w_{ij} 's too high, however, or valuable information will be lost. A useful way to find out where to set the lower limit is to make a plot of the w_{ij} 's as shown in Figure 4-1 for the $C^T C$ matrix.

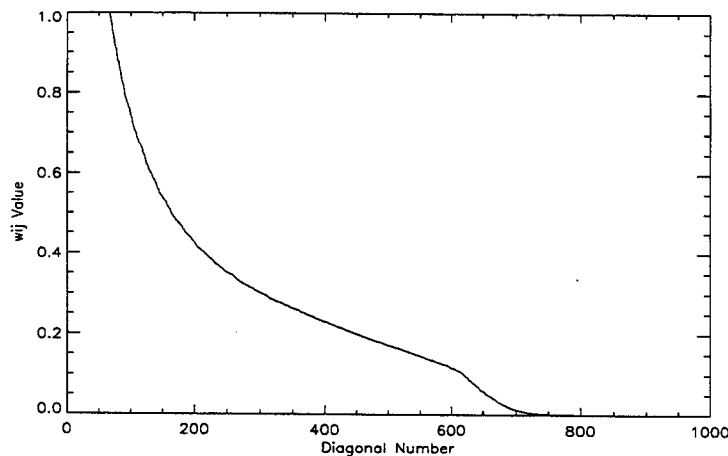


Figure 4-1: The Diagonals, w_{ij} , of the 'W' Matrix

In this figure, the w_{ij} 's fall off smoothly until about $w_{ij} \sim 0.1$ where the falloff becomes rapid (the maximum value of w_{ij} is 15.664 at diagonal number 0). Results of plasma

frame inversions have shown that $w_{ij} \sim .04$ is about the optimum place to set the w_{ij} cutoff (shown in Section 4.3). This balanced the benefits of singular value decomposition (a believable solution) with the data lost by setting a w_{ij} limit (smoothing of the data). $w_{ij} \sim .04$ gives a condition number of $K(C^T C) = 392$. This is in comparison the condition number of $K(C^T C) = 3 \times 10^6$ that one gets if no lower limit is set.

Once a cutoff for w_{ij} has been given, and any elements below it have been set to zero, the inverse of $C^T C$ is simply

$$(C^T C)^{-1} = VWU^T \quad (4.5)$$

4.2 Verification of the Inversion Method

Once a working method for calculating ϵ was in place, it was tested to see if it gave accurate results. An obvious constraint on the solution was non-negativity for the emission power densities. If this criterion was met, it still needed to be shown that the solution given was correct within an acceptable error bound. One way to do this was to set up a test case with known emission to see if the algorithm gave the correct solution. This was done by choosing an emission profile and then converting it to a brightness image with 'C'. The inversion should return a emission profile close to the original. Of course, to be truly general one would have to prove that the algorithm gave acceptable results for all emission profiles. This was not possible, but if the algorithm was tested for a number of cases and reasonable results were obtained, this should be acceptable.

A checkerboard emission pattern was used to test the inversion algorithm and is shown in Figure 4-2. This emission profile was converted to a bitmap using 'C' and the CCD sensitivity. This bitmap is shown in Figure 4-3. The inversion algorithm was then used to convert the bitmap back to an emission profile. This required about

5 seconds of VAX Alpha workstation time. The results of the inversion were good. The inverted emission profile maintained the checkerboard pattern in Figure 4-2, but individual power densities had some degree of error. The average error was less than 1% and the maximum error was around 2.5%.

It must be pointed out that when the singular value decomposition was applied to the $C^T C$ matrix to get C^{-1} for this case, the w_{ij} cutoff (w_{ijmin}) was set to 0. Since the test emission was noiseless data and the pattern was regular, the inversion was not greatly affected by ill-conditioning of the $C^T C$ matrix. It was not possible to let w_{ijmin} be set to 0 for real data, however, because, as will be shown in the next section, the results were not believable. By setting w_{ijmin} at a higher value, it was possible to get reasonable inversion results for real video frames, however, the reconstructed emission profile from the checkerboard pattern bitmap was smoothed somewhat in the divertor slot and underneath the nose of the inner wall. This smoothing increased as the w_{ijmin} was increased, until at high enough values, the entire checkerboard emission pattern was smoothed. This resulted in much lost information, and as a result, the next section will be entirely devoted to optimizing the w_{ij} cutoff so that reasonable emission profiles can be generated from video frames while the effects of smoothing are minimized.

Figure 4-4 shows another test emission pattern that was used to test the inversion procedure, and Figure 4-5 shows the bitmap projected from this information. This emission pattern is a more realistic case than the checkerboard pattern. The results of the inversion were nearly identical to Figure 4-4, with an average error of less than 0.2% and a maximum error of about 1%. The w_{ij} cutoff was also set to zero in this case.

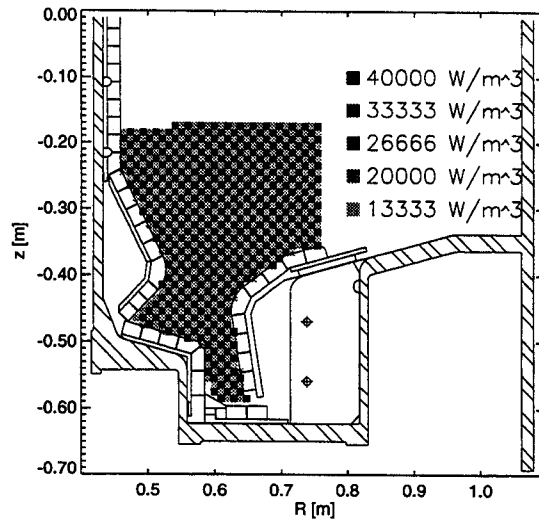


Figure 4-2: Checkerboard Test Emission Profile Used to Test the Video Frame Inversion Procedure

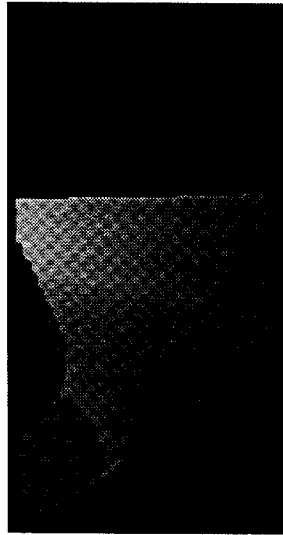


Figure 4-3: 132x251 Bitmap Projected from the Checkerboard Test Emission Profile

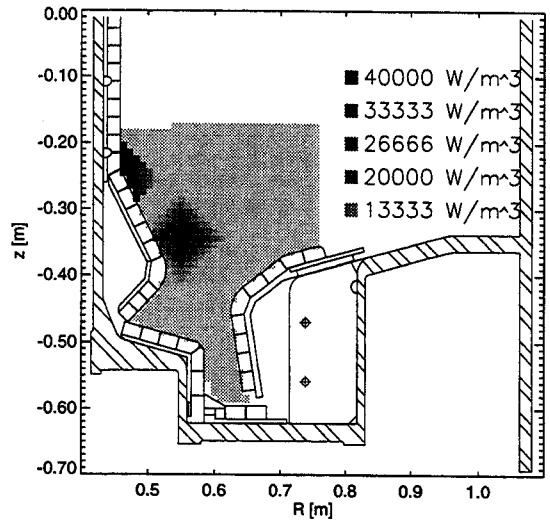


Figure 4-4: A Test Emission Profile Used to Test the Video Frame Inversion Procedure



Figure 4-5: 132x251 Bitmap Projected from the Test Emission Profile

4.3 Optimization of the w_{ij} Cutoff for Inversion of Video Frames

As was discussed in Section 4.1 a large matrix condition number, $K(C^T C)$ could pull the matrix inversion solution far away from its true value. Figure 4-1 showed that w_{ij} fell off smoothly until $w_{ij} \sim .1$ where the values fell off rapidly. The question is, at what value does one set the w_{ij} cutoff (w_{ijmin}) so that it is possible to get believable solution for real data (video frames), while at the same time, not throwing out too much information (oversmoothing the results)?

A video frame from shot 960827014 ([96][08][27][014] = [year][month][day][shot]), shown in Figure 4-6, at a time exposed for .1ms anywhere between 703ms and 736ms ($t = 703-736ms$) was inverted with w_{ijmin} set to 0 (condition number, $K(C^T C) = 3 \times 10^6$). The time the frame was captured was not known any more precisely than this because the CCD camera readout was not synchronized with the start trigger, and as a result there was a 1/30 second (33 ms) uncertainty which depended on how the start trigger corresponded with the exposure time (.1ms in duration) of the camera. The results of a inversion of this frame are shown in Figure 4-7. It can be seen that the emission pattern looks nothing like what one would expect from the frame in Figure 4-6. Also, nearly 40% of the emission power density values were negative, but were made positive in the figure so that the inverted emission profile could be plotted at all. Section 4.2 showed that noiseless test emission cases were not affected by ill-conditioning, but it is obvious that one cannot let the condition number be as large as 3×10^6 for real data.

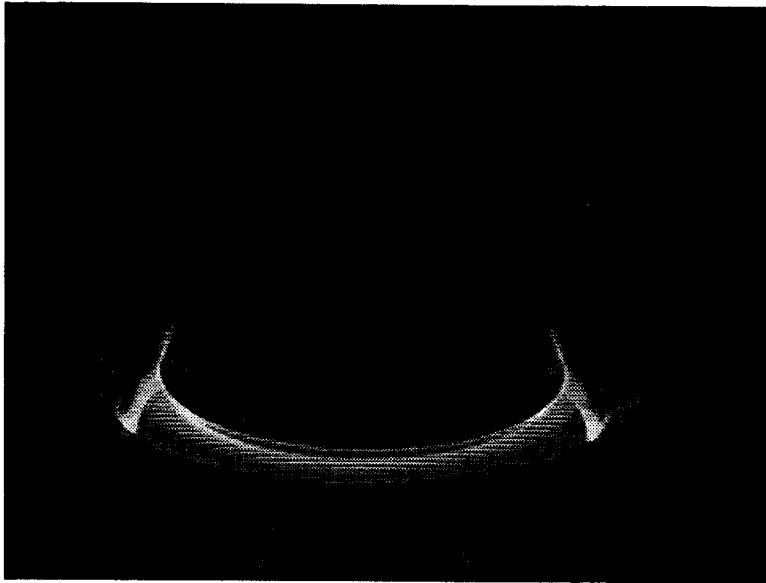


Figure 4-6: Plasma Shot 960827014 at $t = 703\text{-}736\text{ms}$

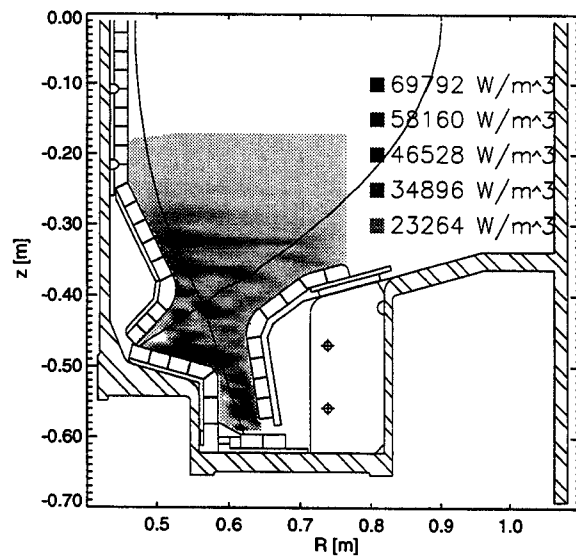
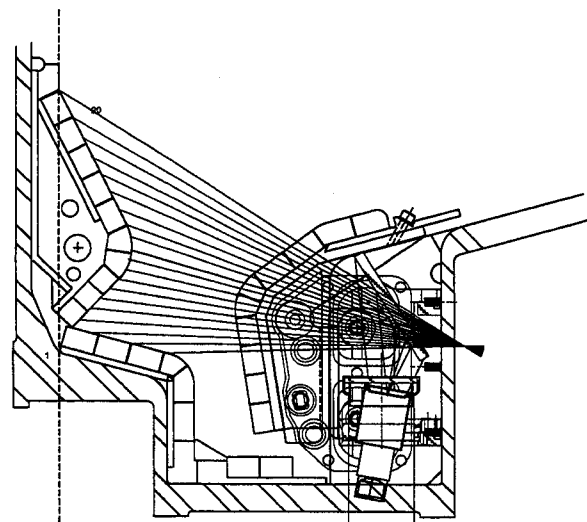


Figure 4-7: Emission Power Density Profile for Shot 960827014 at $t = 703\text{-}736\text{ms}$ with $w_{ijmin} = 0$

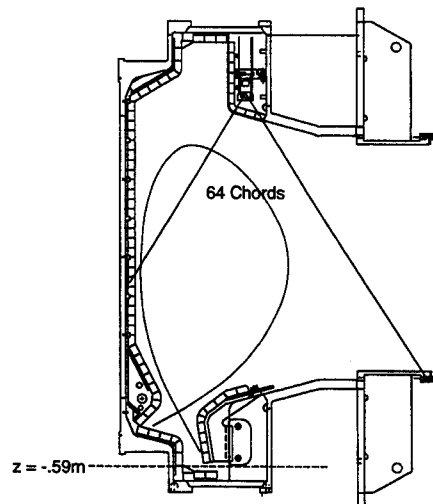
Another way to show that the reconstructed emission profile for shot 960827014 was incorrect for a such a large condition number was to compare it with other diagnostics that viewed D_α emission. The comparison data were taken from two visible light diode reticon arrays filtered for D_α emission [1]. The views of these two arrays are shown in Figure 4-8. Chord brightness data existed for these diodes for the same shot and in the same time range ($t = 703-736\text{ms}$) as the frame from Figure 4-6. To properly do a comparison, it was desirable that the emission be constant in the 33ms of the time range. This was because the framegrabber was not synchronized with the CCD camera and the .1ms exposure time of the CCD camera could have been located anywhere in the 33ms time window. The time that the diode arrays' data were taken was known much more precisely than this ($\pm .5\text{ms}$). The measured diode brightness data was then compared with the inversion results by following the chords from the views in Figure 4-8 through the reconstructed emission power density profile from Figure 4-7 and summing up the brightness along the chords using the equation

$$b_i = \frac{1}{4\pi} \sum_j (\Delta l_{ij} \epsilon_j) \quad (4.6)$$

where Δl_{ij} was the distance a chord, 'i', traveled across an emissivity cell, 'j'. The results of this process can be seen in Figure 4-9 (the inner divertor view) and Figure 4-10 (top view). As shown in these figures, the brightness profiles from the integrated reconstructed emission were very noisy because of the all the negative emission power density values present. In some places in the top array view, the brightness profiles seem similar, but overall, the brightness from the reconstructed emission is incorrect.



(a) Inner Divertor View



(b) Top View

Figure 4-8: Views of the Two Diode Arrays Used to Verify the Inversion Results

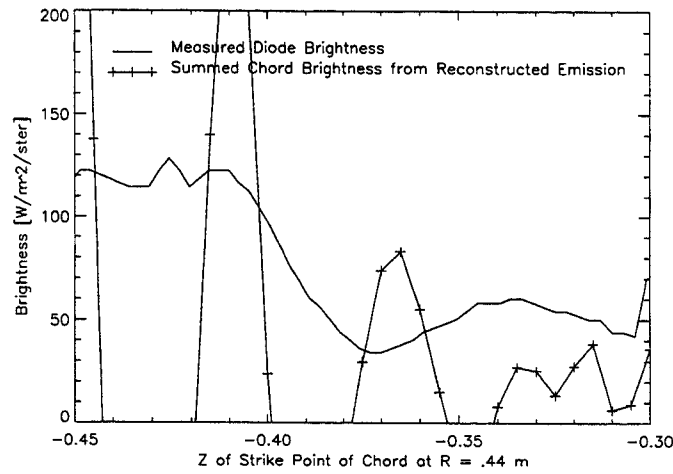


Figure 4-9: Integrated Brightness Along the Chords of the Diode Array Viewing the Inner Divertor for Shot 960827014 at $t = 714\text{ms}$ with $w_{ijmin} = 0$

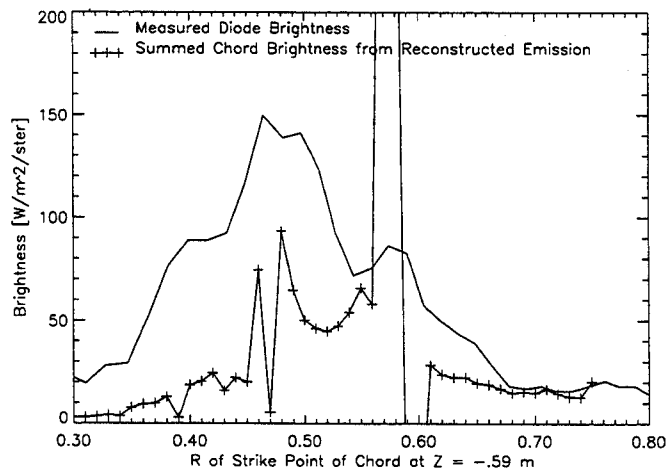


Figure 4-10: Integrated Brightness Along the Chords of the Diode Array Viewing the Plasma from Above for Shot 960827014 at $t = 714\text{ms}$ with $w_{ijmin} = 0$

To get a believable emission profile for shot 960827014 (frame inversions for several other shots will be given in Chapter 5), w_{ijmin} was gradually raised (condition number lowered) in the singular value decomposition algorithm. At each stage, inversions were done both on the test emission profiles and on the actual video frame. Since the test emission profiles were noiseless, and because they were formed directly from the C matrix, inversions done on their projected bitmaps were good measures of how much smoothing was occurring from changes in the condition number. Inversions from the video frame were used to calculate brightness profiles that were compared with the data from the reticon arrays. The condition number was lowered until data from the integrated emission compared favorably with reticon data. This point occurred at $w_{ijmin} \sim .04$ (a condition number of $K(C^T C) \sim 392$).

The results of an inversion of shot 960827014 at $t = 703\text{-}736\text{ms}$ using this condition number are shown in Figure 4-11. The reconstructed emission shown in this figure probably resulted from a combination of emission from recombination [26] and plasma recycling of deuterium at material surfaces. The form of the reconstructed emission seemed to follow the contours of the last closed flux surface (LCFS) rather well, and the emission appeared in reasonable positions around the x-point and strikepoints. The emission appeared here because plasma flows along the field lines terminated in these regions.

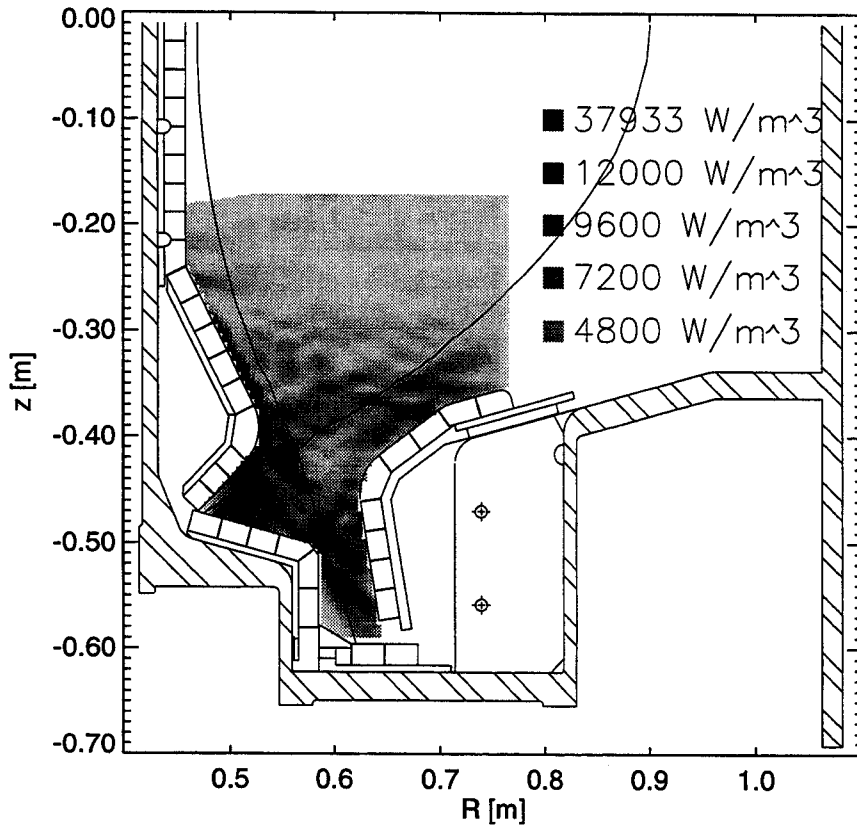


Figure 4-11: Emission Power Density Profile for Shot 960827014 at $t = 703-736\text{ms}$ with $w_{ijmin} = .04$

Figures 4-12 and 4-14 show the smoothing from $w_{ijmin}=.04$ on the inversions of the two test emission patterns from Section 4.2. The checkerboard pattern was a more stringent test of the smoothing because of its highly varying adjacent emission cell values, and this is shown in a maximum percent error of 345% (Figure 4-13) in the divertor slot when compared to the original emission profile. The average error was only 13%, however, so the smoothing was not too extensive. The other test emission pattern (Figure 4-14) did better with a maximum error of 101% in the divertor slot and an average error of 10% as shown in Figure 4-15. Most of the large errors in this case occurred outside of high emission regions, which was encouraging. Both of these reconstructed emission patterns show, that while smoothing has taken place, it is still at acceptable levels except underneath the inner nose and in the bottom of the divertor slot. Reconstructed emission from these regions should not be fully trusted.

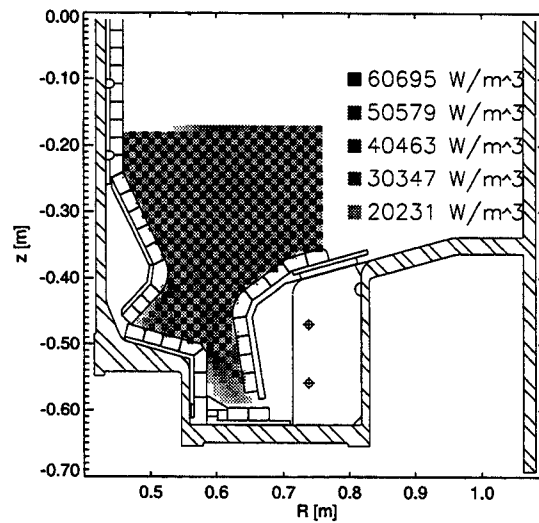


Figure 4-12: Reconstructed Checkerboard Test Emission Profile with $w_{ijmin} = .04$

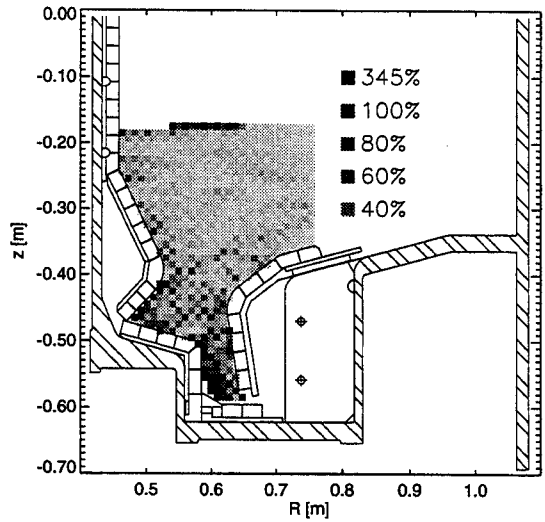


Figure 4-13: Absolute Percentage Difference in the Reconstructed Checkerboard Test Emission Profile with $w_{ijmin} = .04$

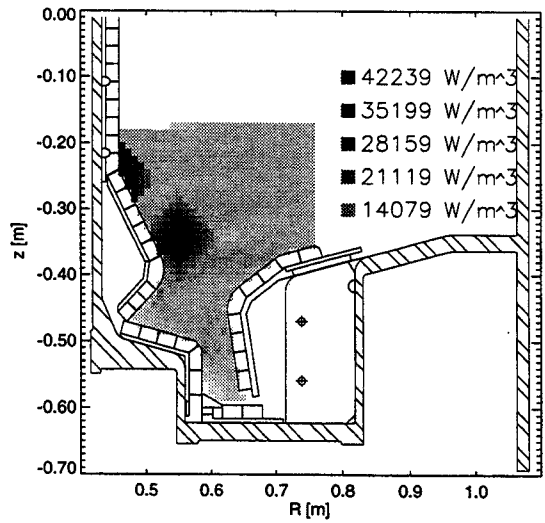


Figure 4-14: Another Reconstructed Test Emission Profile with $w_{ijmin} = .04$

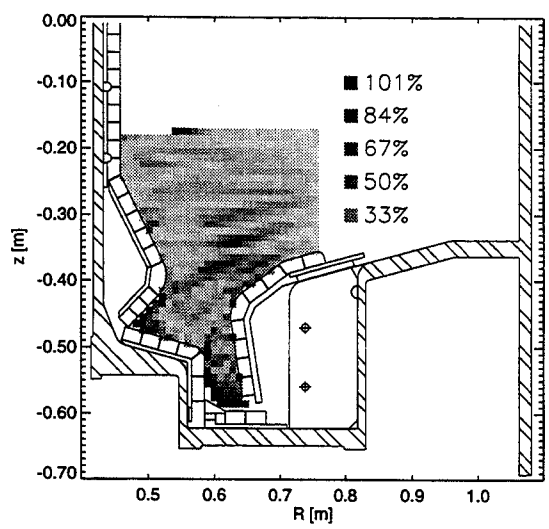


Figure 4-15: Absolute Percentage Difference in the Reconstructed Test Emission Profile with $w_{ijmin} = .04$

The maximum emission power density value in Figure 4-11 of around 38000 W/m^3 was reasonable since another diagnostic on C-Mod using the measured brightness from five arrays of D_α detectors to tomographically reconstruct emission gave emission power densities in the range of $0 - 60,000 \text{ W/m}^3$ for D_α emission on other shots [19], although no tomographic reconstructions existed for the Fall 1996 campaign when the frame used in the inversion was captured.

The 5 seconds required for the inversion of a frame was about the same as was required for the tomographic reconstruction from the D_α detectors. An improvement, however, was that the emission mesh cell size was reduced from $(2\text{cm} \times 2\text{cm})$ to $(1\text{cm} \times 1\text{cm})$ over this older method, and the CCD array sensitivity calibration was much easier to do since there was only one view. The five arrays of D_α detectors required five calibrations and five view determinations.

When the reconstructed emission in Figure 4-11 was summed along the reticon array chords as was done for the $w_{ijmin} = 0$ case, the results were improved. Figures 4-16 and 4-17 show the brightness profiles from the reticon array views from Figure 4-8. Peaks in the chord brightness profiles are located in similar locations for the measured brightness and for the brightness calculated from the reconstructed emission. The heights of the peaks on the left-hand side in these figures are dissimilar, however, by a factor of 2 or more. Some possible explanations for these disparities and possible solutions to them are as follows:

- (1) Boronization [27] of the C-Mod vacuum vessel was begun in the winter of 1995-96. The CCD camera looked into the plasma through a viewing window that was highly exposed to the boron. As a result, a dark coating soon developed on the window that worsened each time the vessel was re-boronized. This lowered the level of brightness seen by the camera (possibly by a factor of 2). A shutter is being put over the window for the next run period. It will be closed during boronization, so that the window will no longer be exposed. The windows that the diode arrays viewed the plasma through

were better protected from the boronization, and as a result, were not coated as much. This could explain the factor of 2 for the peaks on the left-hand side, but the peaks on the right-hand side would then be incorrect by a factor of 2.

(2) Since the tiles on the walls of the Alcator C-Mod vacuum vessel are made of a rather shiny material (molybdenum), one must be concerned with reflections. Reflections will cause the brightness along chords that “see” reflection to be higher than they should be. This could explain the mismatched peak ratios, since “seen” reflection from surfaces is different depending on where one is viewing a light source from. Reflection could be a problem for both the CCD camera view and the reticon array views. The wide angle view of the CCD camera was susceptible to reflections on the outer divertor plates (as was seen in some frames). This could explain both a factor of 2 from the boron coating and the subsequent factor of 2 in the in the right-hand brightness peaks which were located at the outer divertor plate position. This can not be verified until the shutter is put over the viewing window, however, since the mismatched peak ratios could also be explained by reflection seen by the reticon arrays. This could lower their left-hand peaks by a factor of 2, which would mean that the reconstructed emission would be correct as is. Unfortunately a third, and more likely, possibility was that reflection was affecting both the reticons and the CCD arrays. Therefore, reflections must be modelled eventually if the reconstructed emission power density values are to be fully trusted. One way to quantify reflection is to do ray tracings of the CCD viewing pixels by bouncing them off material surfaces a number of times to see where reflection is originating from [28]. This process is rather time consuming, and the reflectivity of the tiles is no longer a constant because of boronization of the vacuum vessel. It may be possible to just bounce the pixel chords once, however, which would cut down on the size of the problem while at least getting a rough estimate of the reflection.

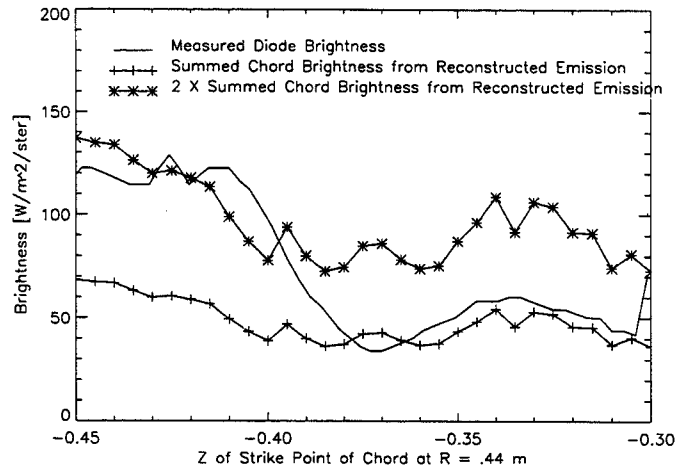


Figure 4-16: Integrated Brightness Along the Chords of the Diode Array Viewing the Inner Divertor for Shot 960827014 at $t = 714\text{ms}$ with $w_{ij} = .04$

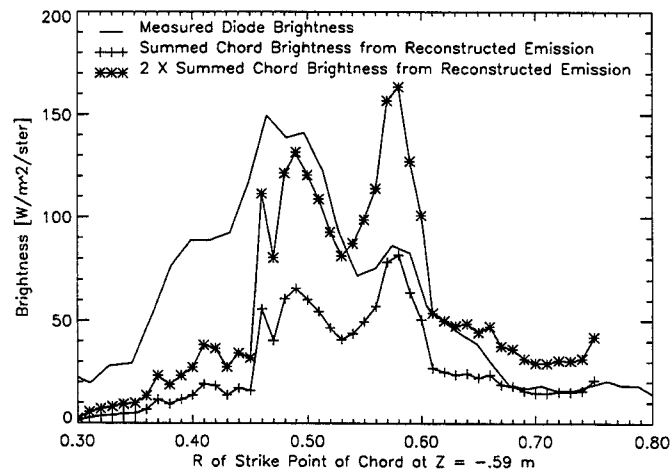


Figure 4-17: Integrated Brightness Along the Chords of the Diode Array Viewing the Plasma from Above for Shot 960827014 at $t = 714\text{ms}$ with $w_{ij} = .04$

4.4 The Effect of 5:1 JPEG Compression on Inversion Results

As was stated in Section 2.3, 5:1 JPEG compression of video frames had little effect on the frames except near sharp pixel value gradients. Figure 4-18 shows the inversion results from an uncompressed frame from shot 960827014 at $t = 703\text{-}736\text{ms}$. Figure 4-19 shows the results of an inversion of the same frame after 5:1 JPEG compression. As can be seen from these two figures, the inverted profiles look nearly identical, although a closer examination revealed that there was some difference in the actual emission power density values. Figure 4-20 shows a profile of the absolute difference between the two inversions. The maximum difference was around 140 W/m^3 (out of typical values of thousands of W/m^3), but most differences were around 20 W/m^3 . Figure 4-21 shows the absolute percentage difference between the two inversions. Most of the differences were less than 5% which means that frames can be 5:1 JPEG compressed with only small errors in frame inversion results. This is good news, because 5:1 compression will allow a week's worth of captured frames to be stored on a single writable CD.

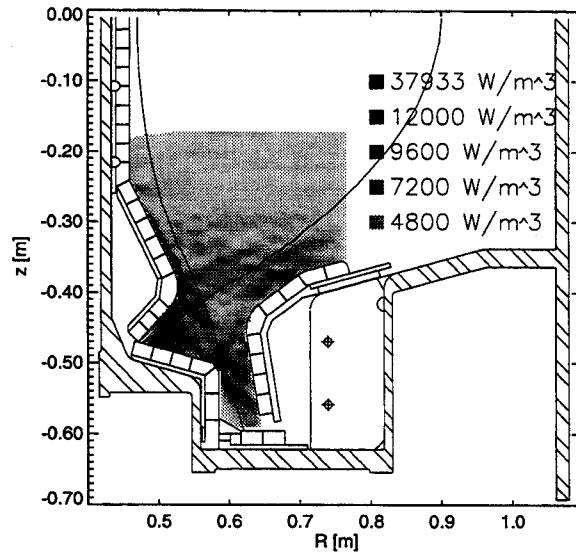


Figure 4-18: The Inversion Results from the Uncompressed Frame from Plasma Shot 960827014 at $t = 703\text{-}736\text{ms}$

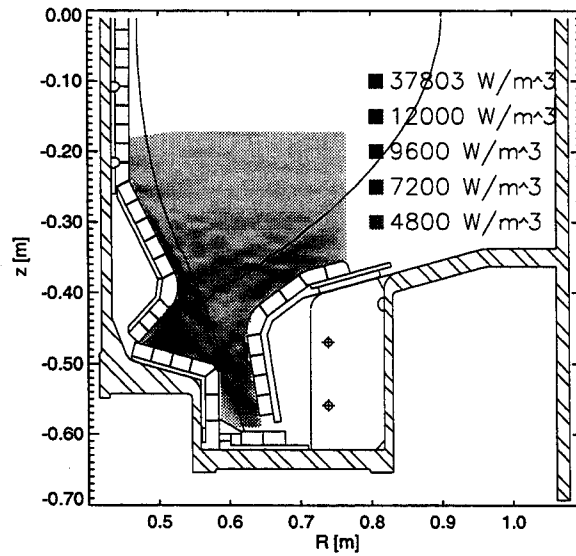


Figure 4-19: The Inversion Results from the 5:1 JPEG Compressed Frame from Plasma Shot 960827014 at $t = 703\text{-}736\text{ms}$

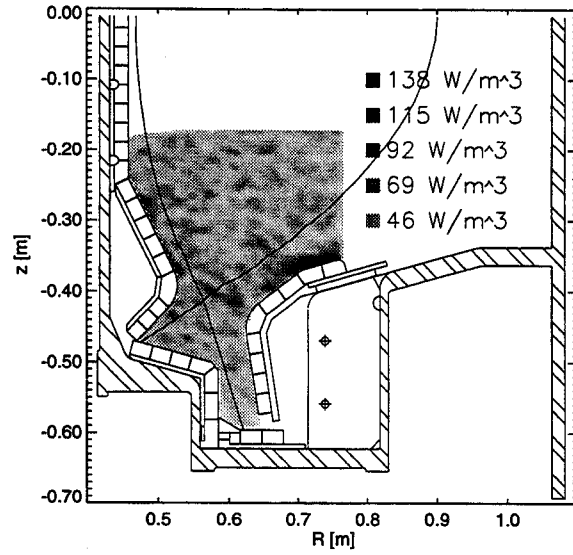


Figure 4-20: The Profile of The Absolute Difference Between the Inversion Results from an Uncompressed Frame vs. a 5:1 JPEG Compressed Frame for Shot 960827014 at $t = 703-736$ ms

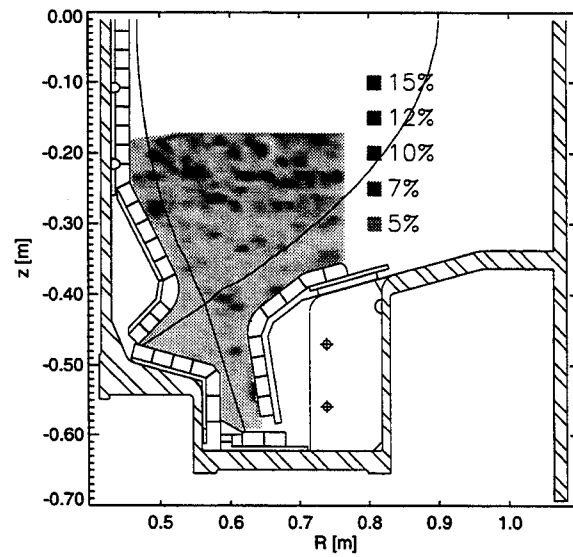


Figure 4-21: The Profile of The Absolute Percentage Difference Between the Inversion Results from an Uncompressed Frame vs. a 5:1 JPEG Compressed Frame for Shot 960827014 at $t = 703-736$ ms

Chapter 5

More Results, Summary, and Future Work

This chapter will give the results from several other reconstructions to further test the inversion method. It will then give a summary of the research outlined in this thesis, and finally, it will speculate on the implications that the inversion procedure may have on visible emission research on Alcator C-Mod.

5.1 More Inversion Results

Most of the frames from Alcator C-Mod's 1996 run period were saturated (pixel values of 245) in the divertor region. Saturation resulted in lower than expected pixel brightness values, because no matter how much emission the viewing chords travelled through, the resulting pixel value could never exceed 245. This saturation problem can be remedied in the next run period by placing neutral density filters over the CCD camera lens which would reduce brightness by a known value. Another remedy is to use a different camera with a self-adjusting gain. The gain for a frame can be measured by examining a narrow white pixel field that is placed on the top of the captured frame by the camera. Its position in the frame can be used to calculate how

much the gain has changed from some known base value.

With the saturation problem, it was not possible to do large-scale analyses of the D_α emission present under different plasma conditions, but such extensive amounts of data existed that it was possible to find a large number of unsaturated frames at various times during plasma discharges. Four examples will be given below, The plasma conditions at the time of frame capture are given, as well as any other useful information. The $C^T C$ matrix used in all inversions was inverted with $w_{ijmin} = .04$.

Figures 5-1 and 5-2: Shot 960828005 at $t = 1037$ - 1070 ms during current flattop. The central electron density was $\bar{n}_e \sim 1.7 \times 10^{20} \text{m}^{-3}$, the plasma current was $I_p = .8\text{MA}$, and the toroidal magnetic field was $B_{Tmax} = 5.4\text{T}$. The beginning of an ELM-free H-mode which lasted from 1028 ms to 1081 ms. Note in Figure 5-2 that the emission is mainly located above the inner strike point and at the outer strike point with very little emission around the x-point. Discharge ended at 1500 ms.

Figures 5-3 and 5-4: Shot 960828005 at $t = 1070$ - 1103 ms during current flattop. The central electron density was $\bar{n}_e \sim 1.9 \times 10^{20} \text{m}^{-3}$ and the plasma current was $I_p = .8\text{MA}$. After or at the transition out of H-Mode. Many of the pixels in Figure 5-3 are saturated. Observe the reflection on some of the outer divertor plates. Note in Figure 5-4 how the emission on the inner wall has extended vertically, and has spread out horizontally. Still very little emission around the x-point. The emission on the outer divertor plate may be due to reflection, except around the outer strike point which is probably real. Discharge ended at 1500 ms.

Figures 5-5 and 5-6: Shot 960820016 at $t = 270$ - 303 ms during current rise. The central electron density was $\bar{n}_e \sim 1.4 \times 10^{20} \text{m}^{-3}$ and the plasma current was $I_p \sim .75\text{MA}/.80\text{MA}$. Note how the emission is concentrated on the inner wall and on the outer divertor plates near the strike points. Observe that emission is located on the inboard side of the x-point, but that there is very little on the outboard side of the x-point. Discharge ended at 1500 ms.

Figures 5-7 and 5-8: Shot 960830009 at $t = 837\text{-}870\text{ms}$ during current rampdown. The central electron density was $\bar{n}_e \sim 1.8 \times 10^{20} \text{m}^{-3}$, the plasma current was $I_p \sim .50\text{MA}/.80\text{MA}$, and toroidal magnetic field was $B_{Tmax} = 5.3\text{T}$. Prior to a disruption at 911ms. Note how the plasma is no longer diverted and how emission above the outer divertor plates has filled in the region below the limited LCFS.

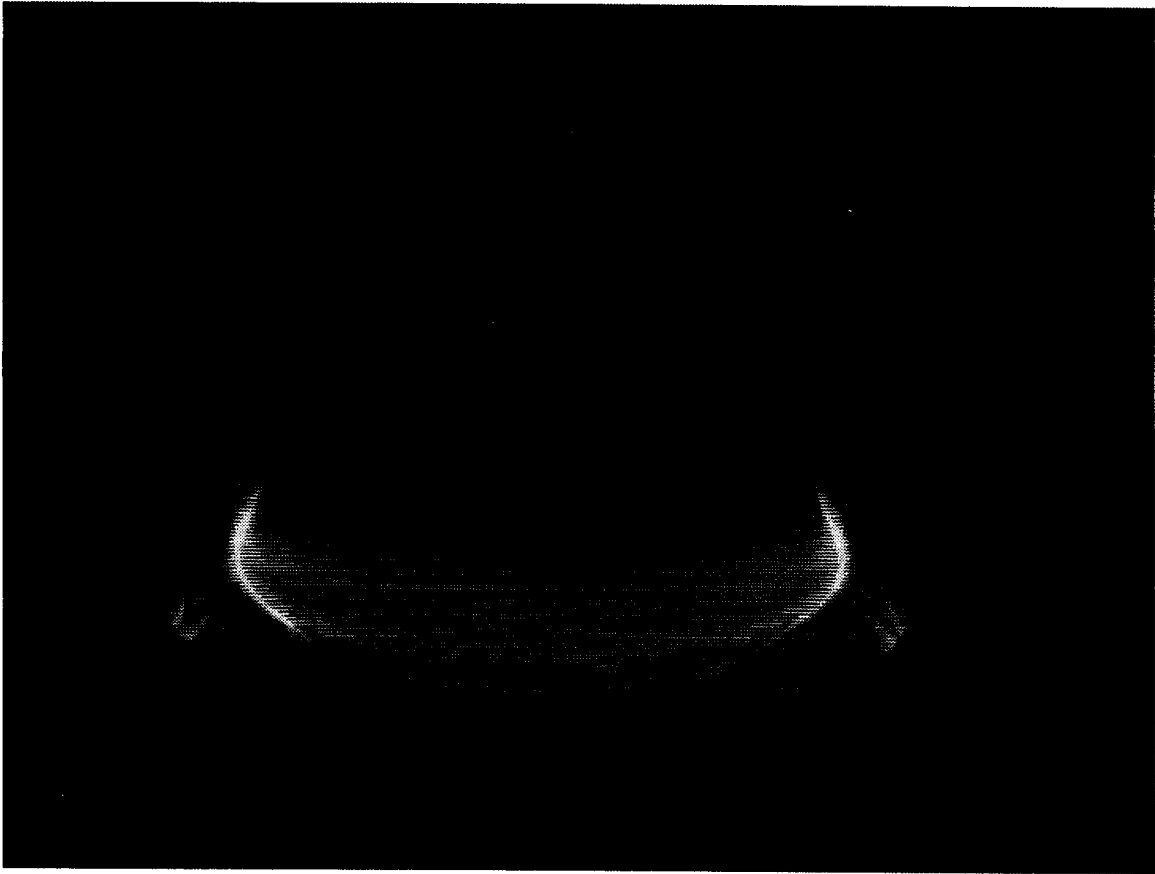


Figure 5-1: Shot 960828005 at $t = 1037-1070\text{ms}$

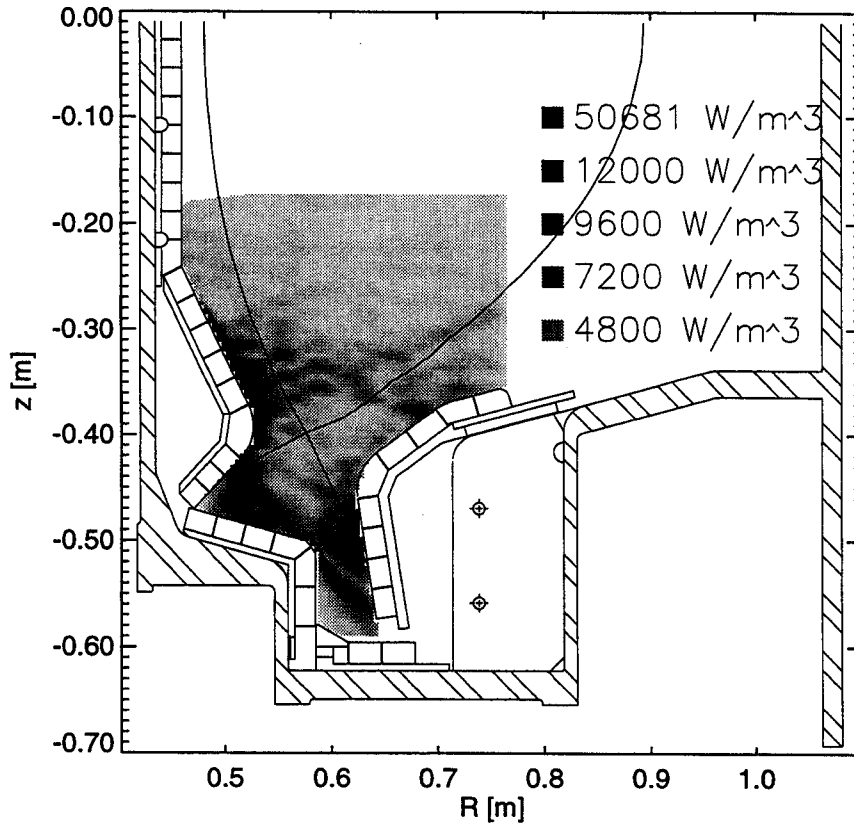


Figure 5-2: Emission Power Density Profile for Shot 960828005 at $t = 1037-1070\text{ms}$. Comments: during current flattop; $\bar{n}_e \sim 1.7 \times 10^{20} \text{m}^{-3}$; $I_p = .8 \text{ MA}$; $B_{Tmax} = 5.4\text{T}$; beginning of an ELM-free H-Mode that lasted from 1028-1081ms; shot ended at 1500 ms

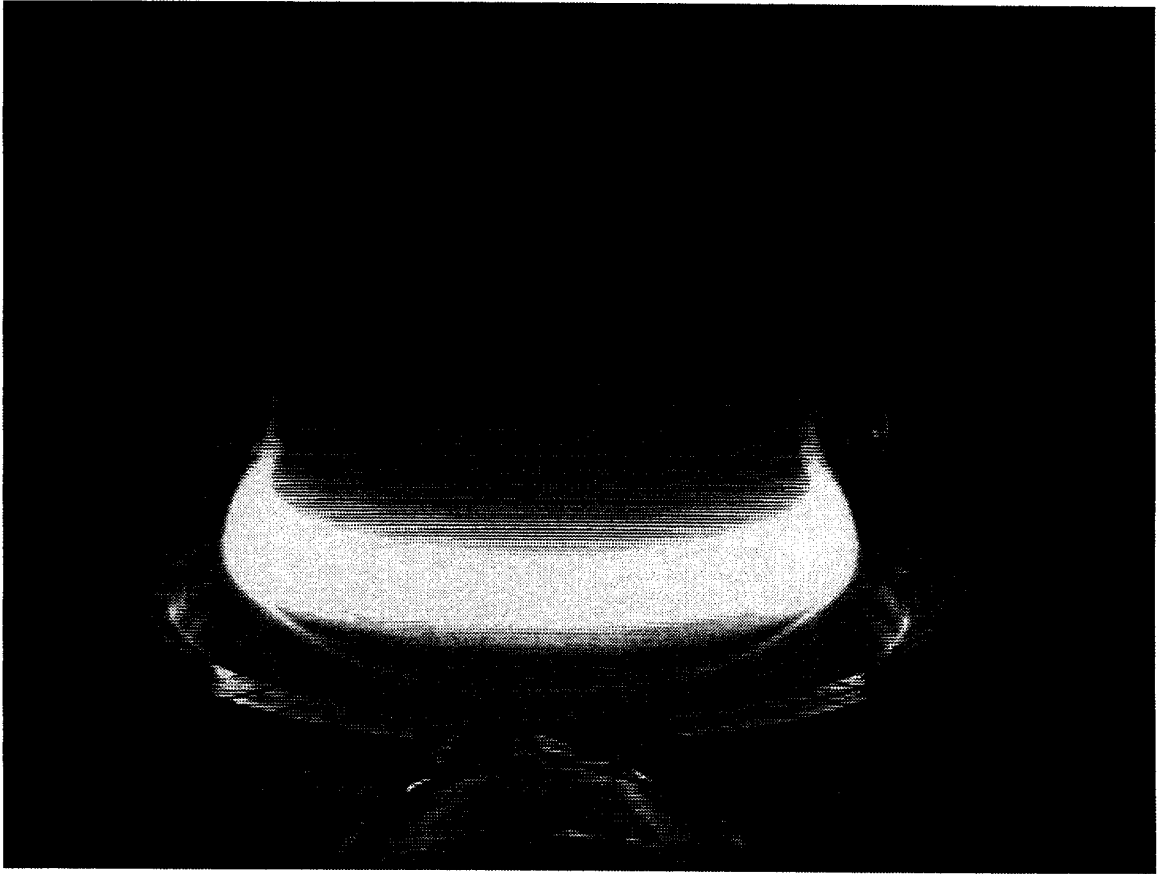


Figure 5-3: Shot 960828005 at $t = 1070-1103\text{ms}$

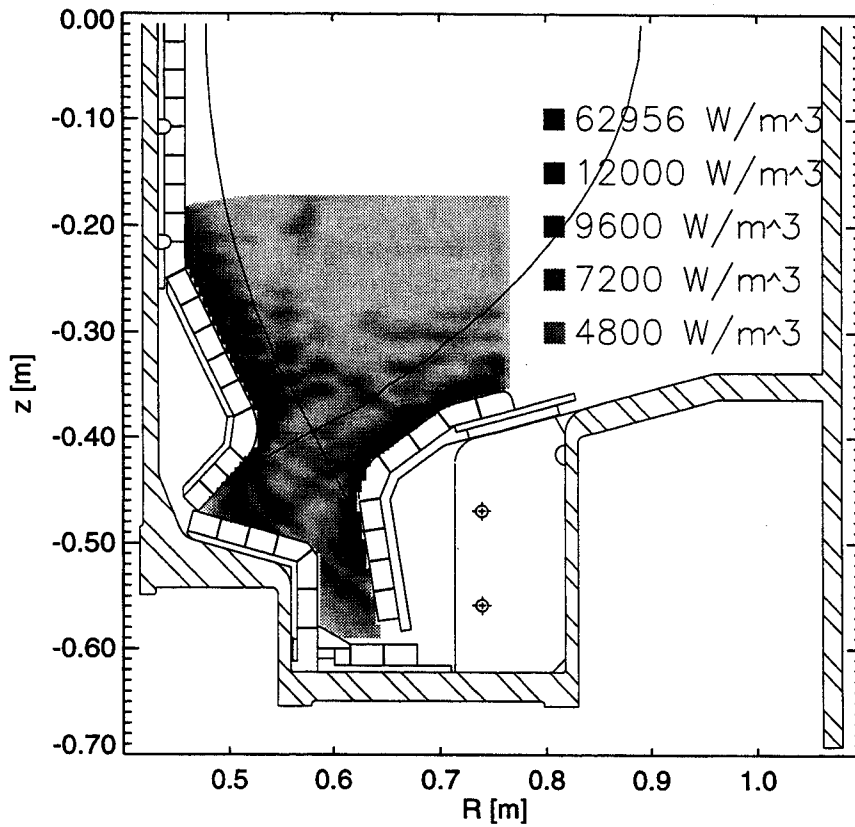


Figure 5-4: Emission Power Density Profile for Shot 960828005 at $t = 1070-1103$ ms. Comments: during current flat-top; $\bar{n}_e \sim 1.9 \times 10^{20} m^{-3}$; $I_p = .8$ MA; $B_{Tmax} = 5.4$ T; after or at the transition out of H-mode; shot ended at 1500 ms.

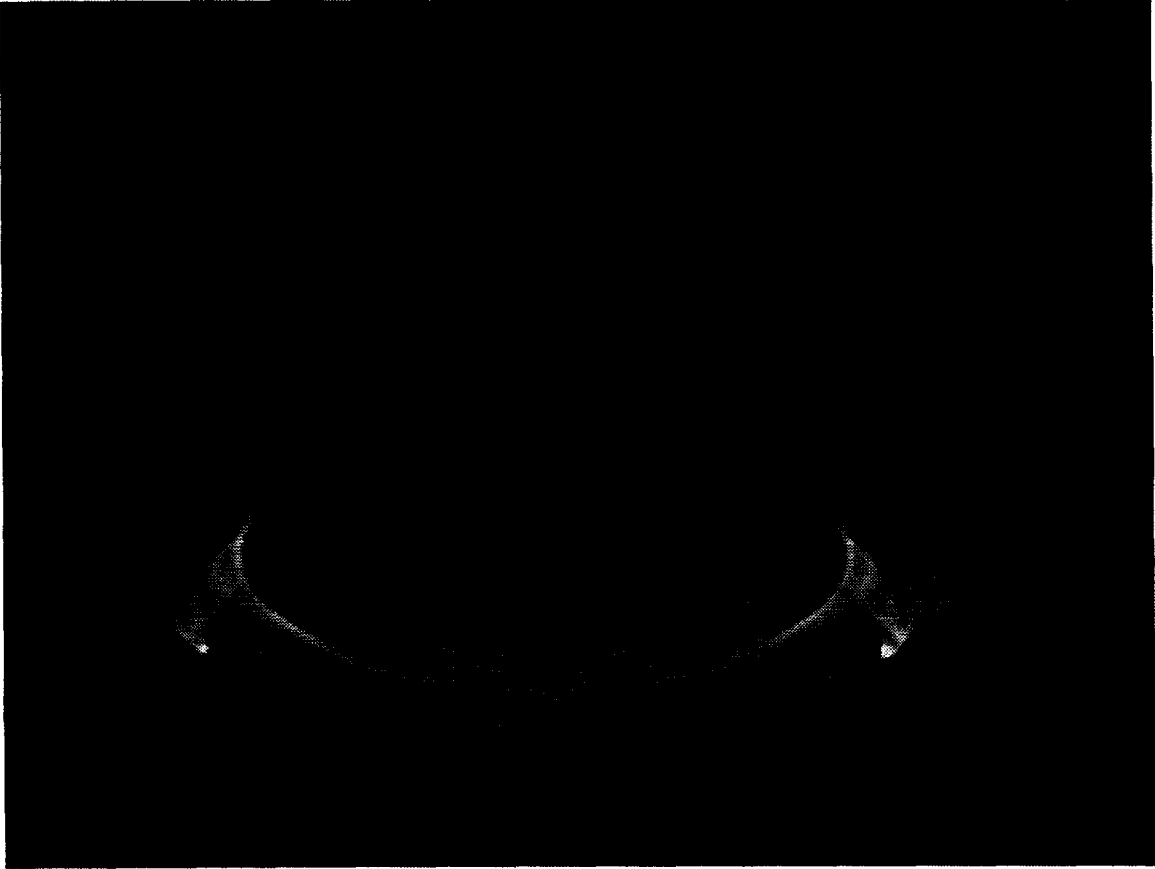


Figure 5-5: Shot 960820016 at $t = 270\text{-}303\text{ms}$

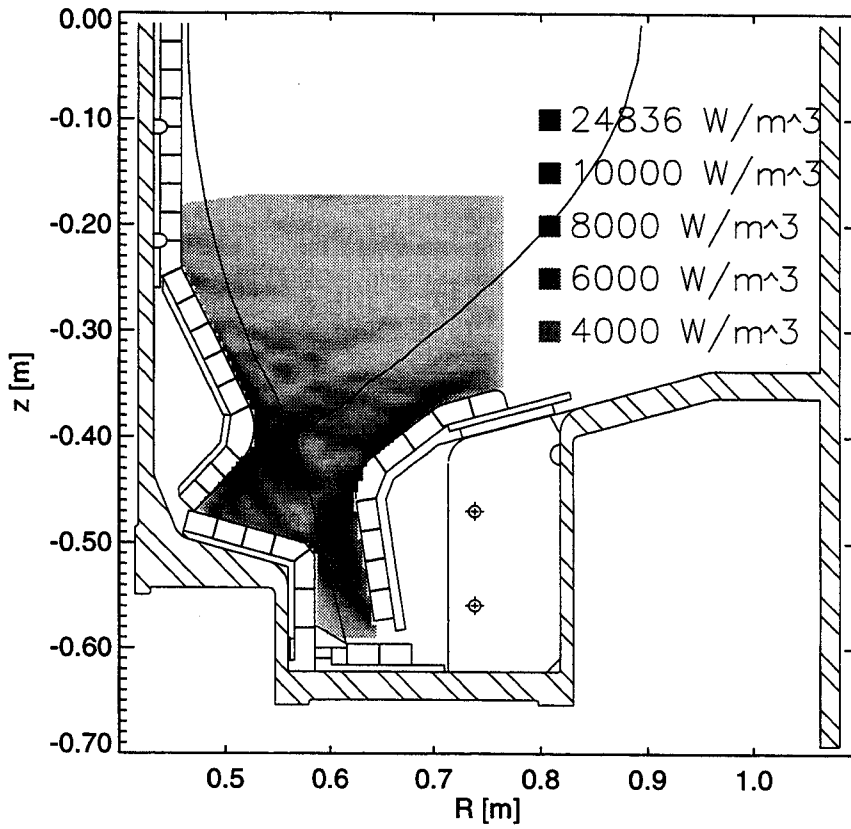


Figure 5-6: Emission Power Density Profile for Shot 960820016 at $t = 270\text{-}303\text{ms}$. Comments: during current rampup; $\bar{n}_e \sim 1.4 \times 10^{20} \text{m}^{-3}$; $I_p \sim .75\text{MA}/.80 \text{MA}$; shot ended at 1500ms.



Figure 5-7: Shot 960830009 at $t = 837\text{-}870\text{ms}$

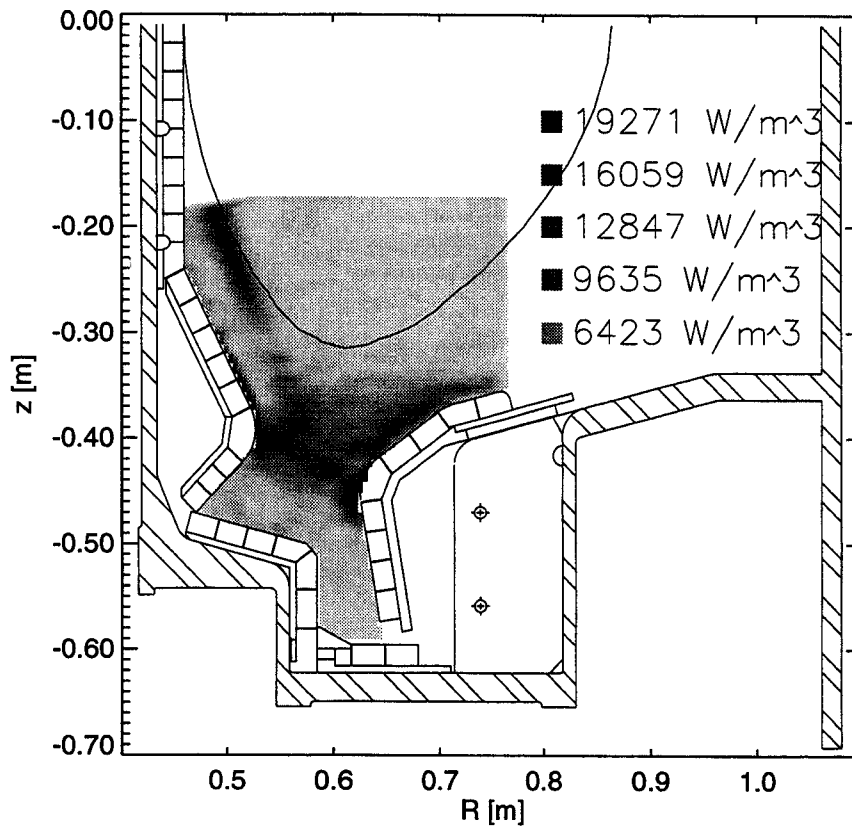


Figure 5-8: Emission Power Density Profile for Shot 960830009 at $t = 837-870\text{ms}$. Comments: during current rampdown; $\bar{n}_e \sim 1.8 \times 10^{20} \text{m}^{-3}$; $I_p \sim .50\text{MA}/.80\text{MA}$; $B_{Tmax} = 5.3\text{T}$; prior to a disruption at 911 ms

5.2 Summary

The video capture, storage, and retrieval system is a robust system that is being used routinely to obtain video images from C-Mod plasma discharges. The geometry of one of the camera views with respect to tokamak geometry has been determined. Also, the CCD detector-based camera, which was filtered for D_α emission, has been absolutely calibrated to yield source brightness. To calculate the emission power density profiles present in the plasma from brightnesses measured in the CCD frames, i.e. ϵ in

$$b = \frac{1}{4\pi} \int_{l.o.s.} \epsilon(l) dl \quad (5.1)$$

the brightness equation was discretized

$$b_i = \frac{1}{4\pi} \sum_j C_{ij} \epsilon_j \quad (5.2)$$

into a 132×251 (i) region of frame pixels and a 32×42 (j) region of emission cells covering the lower part of the plasma including the divertor. ϵ_j is the discretized emission power density in units of $[W/m^3]$. The elements, C_{ij} , are the discretized differential lengths (Δl_{ij}) of frame pixel chords across emission cells along each pixel's line-of-sight. C has been calculated for the 132×251 region of pixels. This matrix was very large (19317×811) but was relatively sparse ($\sim 2\%$ populated) so it was stored in a compressed state. Since C^{-1} was not sparse, however, so it could not be calculated directly to solve for ϵ because of computer memory and storage constraints. By multiplying both sides of the above discretized equation by C^T , however, one could solve for ϵ to get

$$\epsilon = 4\pi(C^T C)^{-1} C^T b \quad (5.3)$$

C^T was stored in a compressed form and $(C^T C)^{-1}$ was stored in an uncompressed form. This solved the storage problem because $(C^T C)^{-1}$ was only a 811x811 matrix. The inverse of $C^T C$ was calculated after applying a singular value decomposition, since the matrix was very poorly conditioned.

Two “test emission” profiles were set up to test the inversion algorithm, and the inverted emission values were within $\pm 1\%$ of test emission values on average. The frame inversions required about 5 seconds of VAX Alpha workstation time. The emission profiles were obtained by setting the w_{ij} cutoff (w_{ijmin}) in the singular value decomposition to 0. This resulted in a large matrix condition number of 3×10^6 . This was not a problem for the test emission profiles, since they were noiseless and formed directly from the C matrix. This condition number was too large for inversions of actual video frames, however, because inverted emission power density values were noisy with a large number of negative values. As a result, w_{ijmin} was raised to try and improve the results. This essentially smoothed the data. This smoothing could be seen quite clearly in the divertor slot and underneath the inner nose in inversions of the test emission profiles. Analysis was done to find the optimum w_{ijmin} that allowed reasonable reconstructed emission values while minimizing smoothing.

To determine whether the reconstructed emission values were reasonable, the emission power density profile was summed along viewing chords from two visible light diode reticon arrays that viewed the plasma from different locations using Equation 5.2. C_{ij} (Δl_{ij}) was the distance that viewing chords travelled across emission mesh cells from the reconstruction along the line-of-sight. This resulted in calculated brightness values for the diode detector viewing chords that could be compared with actual brightness data taken from the detectors for the same shot and in the same time range as the

frame used in the inversion (The emission must not be changing very much during the time range since the time that the frame was captured is only known within ± 17 ms). By slowly increasing the w_{ij} cutoff value, it was possible to get brightness profiles from the reconstructed emission that were similar to the diode profiles, while minimizing the smoothing seen in reconstructions of the two test emission profiles. It was found that a w_{ij} cutoff of $\sim .04$ (a condition number of ~ 392) accomplished this.

While the brightness profiles calculated from reconstructed emission were similar to the reticon measurements, disparities existed. Some of the calculated brightness peaks were smaller by a factor of ~ 2 when compared with the reticon values. It was speculated that a dark coating over the CCD camera viewing window, formed from boronizations of the C-Mod vacuum vessel, might be partially responsible. Reflections from the shiny molybdenum plasma facing tiles were also believed to be causing brightness peaks to be larger than they should be in some areas. It is difficult to separate the effects of boronization of the window and reflections, but a shutter is being installed over the camera viewing window for the next C-Mod campaign that will be closed during boronizations. This should simplify matters, but reflections must still be modelled, since the CCD array and the reticon arrays were both susceptible to reflections, and it was difficult to know which brightness values could be absolutely trusted.

The inverted emission profiles were also compared with profiles tomographically reconstructed from data taken from five D_α detectors already in place. Although no direct comparisons were possible, because no tomographic reconstructions were available from the 1996 campaign, it was still possible to get a rough idea of the emission power density values that one would expect. The results of this comparison were encouraging. Emission power density values calculated from the inversion procedure fell within a range of values ($0 - 60,000 \text{ W/m}^3$) usually seen in the tomographic reconstructions. The video frame inversion time of ~ 5 seconds was nearly the same as the time required for the tomographic reconstruction, but the emission mesh cell

size was reduced from (2cm x 2cm) to (1cm x 1cm). Also, the CCD array's viewing geometry and sensitivity were much easier to calculate than the tomography system which required five separate calculations from the five different views.

It was found that 5:1 JPEG compression of video frames had little effect on inversion results. Differences were below 5%, in general. This level of compression would allow a week's worth of Alcator C-Mod shot data to be stored on a single writable CD while not losing too much information.

5.3 Future Work

Since the molybdenum facing tiles in the tokamak are shiny, the effect of reflection on inversion results must be quantified. Reflection was sometimes a problem for the outer divertor plates which could reflect the bright emission often seen on the inner nose of the tokamak (e.g. Figure 5-3). Some analysis must be done to see whether emission on the outer divertor plates in reconstructions is real or not, and if it is real, what its true values are.

Given the short time needed for inversion of a video frame (~ 5 sec), many possibilities exist for future work on the inversion procedure. Since the reconstruction only covered the lower third of the plasma column, this region could be extended upwards if desired. This would greatly increase the size of the problem, but there are a number of things that can be done to optimize the problem. If the amount of storage needed or the time of inversion becomes too large, one might reduce the emission mesh resolution or throw out some of the pixel chords, since, as was determined in Section 3.5, the problem is greatly overdetermined for some emission cells.

Since the time between plasma shots on Alcator C-Mod is around 20 minutes, and due to the fact that the inversion of an entire shot (45 frames) would only take about 4 minutes, the possibility exists to invert the frames from a plasma discharge "on the fly" between shots. Thus, this information could be used as feedback for the day's

experiment if required. Even though the captured frames would still have to be stored on a dedicated PC (and eventually CD) because of their great size, the emission power density results could be stored directly in the C-Mod shot archive. This is possible because an entire shot's emission information would only require ~ 140 kB of storage (the disk space needed to store 811×45 emission cell values).

As was shown in Figure 3-18, most of the pixels in the wide angle view were not used. Therefore, it would be beneficial to use a lens with a longer focal length. This would allow the region used in the reconstruction to fill the entire frame. A longer focal length ($\gtrsim 8$ mm) would greatly reduce the lens distortion problem, and filling the entire frame would allow the emission mesh resolution to be reduced to the millimeter level. This would be an important improvement, since it would be possible to see visible emission regions in much greater detail.

The wide angle view from which captured frames were inverted in this thesis was filtered for the D_α wavelength using a wide bandpass colored glass filter combination. Narrow field of view lenses (longer focal lengths) can be filtered with standard interference filters. Views can be filtered for helium, carbon, boron, oxygen, etc. Carbon and oxygen emission would be particularly useful in studies of MARFE's^a [7, 8].

Given these and other possibilities, the inversion procedure described in this thesis should prove to be useful and may lead to even more exciting possibilities than those described here.

^aMultifaceted Asymmetric Radiation From the Edge

Appendix A

Steps Required to Invert Video Frames to Get Corresponding Emission Power Density Profiles

The path that one needs to take to calculate emission power density profiles from video frame brightness data is long and involves the use of a number of algorithms. To facilitate this process for other users who wish to invert the emission from new camera views, step-by-step instructions will be given here. The form of the dialog will be as follows:

Step N

Action to be Taken:

Required Algorithms:

Necessary Input:

Algorithm Output:

Note: All output is stored in the directory `CMOD2$DKA300:[VIDEO]`

Step I

Action to be Taken: Determine the camera view

Required Algorithms: USER9:[ALLEN.PROGRAMS]CAMERA_ASIDE.PRO

Necessary Input: (1) A frame from the view that will be used in the inversion, (2) the R , z , and θ coordinates of known and seen objects in the frame, (3) the x and y coordinates of known and seen objects in the frame, (4) modelled lens distortion corrections if necessary, (5) the location of the central pixel in the frame and the yaw, pitch, and roll of the camera, (6) the location of the camera in tokamak geometry and the lens focal length.

Algorithm Output: The algorithm will output the entered frame with the calculated position of known and seen objects plotted on the frame. Entered parameters must be modified until the calculated positions match the actual positions in the frame. Used in conjunction with FIND_ALPHA_COR.PRO (See Step II) to model the camera view geometry correctly.

Step II

Action to be Taken: Determine the lens distortion correction

Required Algorithms: USER9:[ALLEN.PROGRAMS]FIND_ALPHA_COR.PRO

Necessary Input: (1) The R , z , and θ coordinates of known and seen objects in the frame, (2) the x and y coordinates of known and seen objects in the frame, (3) the camera parameters (focal length, camera position, etc.).

Algorithm Output: This algorithm uses the positions of known and seen objects to calculate the lens distortion present in video images. It fits the differences found in the ray angles (from the central ray of the lens) between objects in image space and object space to a third order polynomial. This fit allows one to travel correctly from image to object space and vice versa with lens distortion present. Used in conjunction with CAMERA_ASIDE.PRO to model the camera view geometry correctly.

Step III

Action to be Taken: Calculate the C matrix to be used in the inversion

Required Algorithms: USER9:[ALLEN.PROGRAMS]CALC_GEOM.PRO

Necessary Input: (1) The camera parameters, (2) the modelled distortion corrections, (3) the emission mesh geometry, (4) the range of pixels that cover the emission mesh region.

Algorithm Output: This algorithm follows pixel chords through the Alcator C-Mod tokamak geometry and determines the path length that the viewing chords travel across emission cells (the C matrix). It stores the C matrix in a compressed form with no pathlengths of zero saved. FMESHT(i) is the frame pixel number, DMESHT(i) is the emission cell number, and DELTALT(i) is the pathlength across DMESHT(i) on the pixel chord FMESHT(i).

Step IV

Action to be Taken: Puts the compressed C matrix in two different forms to speed up matrix multiplication and calculates the $C^T C$ matrix.

Required Algorithms: USER9:[ALLEN.PROGRAMS]FORM_MATRICES.PRO

Necessary Input: FMESHT, DMESHT, DELTALT

Algorithm Output: This algorithm gives FMESHT and DMESHT one-to-one correspondence, since one frame pixel chord can cross the same emission cell more than once. The DELTALT's of repeated emission cells are simply added together and stored as one value. This results in FMESH1, DMESH1, DELTAL1 which are stored in order of increasing pixel number. The algorithm also makes FMESH2, DMESH2, and DELTAL2 which contain the same information as FMESH1, DMESH1, and DELTAL1 but are stored in order of increasing emission cell number. The reason that this is done is because matrix multiplication is made faster if the compressed C matrix is stored in readily usable forms. START1 and FINISH1 are also created.

These are two vectors that are indexed by FMESH1(i) value and give the starting element number (i_{start}) and the ending element number (i_{finish}) of entries in FMESH1 for a given pixel. This greatly speeds up row multiplication when multiplying matrices by utilizing the sparseness of the C matrix (i.e. no elements with a value of 0 are multiplied). Two other vectors, START2 and FINISH2, are created for a similar purpose, but they operate on DMESH2. Finally, the algorithm uses FMESH's, DMESH's and DELTAL's to calculate the $C^T C$ matrix.

Step V

Action to be Taken: Use singular value decomposition to invert the $C^T C$ matrix.

Required Algorithms: USER9:[ALLEN.PROGRAMS]SING_VAL_DEC.PRO

Necessary Input: (1) The $C^T C$ matrix, (2) the lowest w_{ij} value that one will accept

Algorithm Output: $(C^T C)^{-1}$

Step VI

Action to be Taken: Make a test emission profile and the corresponding projected bitmap to test the inversion algorithm.

Required Algorithms: USER9:[ALLEN.PROGRAMS]MAKE_TEST_EMISS.PRO

Necessary Input: (1) A desired emission profile, (2) the C matrix

Algorithm Output: This algorithm uses the test emission profile and the C matrix to create a projected bitmap of the emission. It saves the test emission as TEST_EMISS and the corresponding bitmap as TEST_BMP.

Step VII

Action to be Taken: Invert real bitmaps and test bitmaps to get emission profiles

Required Algorithms: USER9:[ALLEN.PROGRAMS]FIND_EMISS.PRO

Necessary Input: (1) The bitmap that one wishes to invert, (2) the calculated sensitivity of the CCD array.

Algorithm Output: This algorithm inverts the entered bitmap to get an emission power density profile.

Step VIII

Action to be Taken: Plot inverted and test emission profiles

Required Algorithms: USER9:[ALLEN.PROGRAMS]PLOT_EMISS.PRO

Necessary Input: Enter the emission profile that one wishes to plot.

Algorithm Output: This algorithm plots the entered emission profile to the screen or to a PostScript file.

Bibliography

- [1] J.L. Terry, J.A. Snipes, and C. Kurz. *Rev. Sci. Instrum.*, 66(1):555, 1995.
- [2] C. Kurz, et al. *Rev. Sci. Instrum.*, 66(1):619, 1995.
- [3] P.C. Stangeby and G.M. McCracken. Plasma Boundary Phenomena in Tokamaks. *Nuclear Fusion*, 30(7):1226, 1990.
- [4] P. Bogen and E. Hintz. Plasma Edge Diagnostics Using Optical Methods. In *NATO ASI Series: Physics of Plasma-Wall Interactions in Controlled Fusion*, volume 131, pages 216–229, October 1986.
- [5] F. Engelman. Approaches to Controlled Fusion and Role of Plasma-Wall Interactions. In *NATO ASI Series: Physics of Plasma-Wall Interactions in Controlled Fusion*, volume 131, page 32, October 1986.
- [6] J.A. Goetz, et al. Comparison of Detached and Radiative Divertor Operation in Alcator C-Mod. *Phys. Plasmas*, 1995.
- [7] I.H. Hutchinson. Thermal Front Analysis of Detached Divertors and Marfes. *Nuclear Fusion*, 1994.
- [8] P.C. Stangeby and G.M. McCracken. Plasma Boundary Phenomena in Tokamaks. *Nuclear Fusion*, 30(7):1321, 1990.
- [9] U. Ascoli-Bartoli. High- and Low-Density Plasma Experiments within the MIT Alcator Programme. *Plasma Phys. Control. Fusion*, 38:1213–1223, 1996.
- [10] S. Fairfax, et al. Papers Presented at the IEEE 14th Symposium on Fusion Engineering. Technical Report PFC/JA-91-33, MIT Plasma Fusion Center, 175 Albany Street, Cambridge, MA 02139, October 1991.
- [11] M. Greenwald, et al. H-mode Confinement in Alcator C-Mod. Technical Report PFC/JA-96-29, MIT Plasma Fusion Center, 175 Albany Street, Cambridge, MA 02139, September 1996.
- [12] J.A. Goetz, R.S. Granetz, B. Lipschultz, and R. Nachtrieb. Radiation Emissivities in the Alcator C-Mod Divertor. In *Bulletin of the American Physical Society*, volume 39, page 1670, November 1994.

- [13] B. LaBombard, et al. Scaling and Transport Analysis of Divertor Conditions on the Alcator C-Mod Tokamak. *Phys. of Plasmas*, 2(6):2242–2248, June 1995.
- [14] D.F. Jablonski. *Local Gas Injection as a Scrape-off Layer Diagnostic on the Alcator C-Mod Tokamak*. Ph.D. Thesis, Massachusetts Institute of Technology, June 1996.
- [15] P.C. Stek and J. Irby. Reflectometry on Alcator C-Mod. In *IAEA Technical Meeting in Microwave Reflectometry for Fusion Plasma Diagnostics*, 1994.
- [16] A. Niemczewski, B. Lipschultz, B. LaBombard, and G. McCracken. In-situ Neutral Pressure Measurements in a Compact High-Field Tokamak. *Rev. Sci. Instrum.*, January 1995.
- [17] A.J. Allen, et al. The High Resolution Video Capture System on the Alcator C-Mod Tokamak. *Rev. Sci. Instrum.*, January 1997.
- [18] Steve Horne. Personal Communication, 1996.
- [19] C. Kurz. *Tomography of Light Emission from the Plasma Edge of the Alcator C-Mod Tokamak*. Ph.D. Thesis, Massachusetts Institute of Technology, May 1995.
- [20] M.V. Kline. Optics. March 1970.
- [21] L.L. Lau, et al. *Nuclear Fusion*, 25:1611, 1985.
- [22] M.E. Fenstermacher, et al. A Tangentially Viewing Visible TV System for the DIII-D Divertor. *Rev. Sci. Instrum.*, January 1997.
- [23] F. Alvarado. The Sparse Matrix Manipulation System. 1986.
- [24] W.H. Press, et al. Numerical Recipes in C: The Art of Scientific Computing. pages 52–59, March 1986.
- [25] *IMSL Math/Library Version 2.0*, volume 1. September 1991.
- [26] D. Lumma, J.L. Terry, and B. Lipschultz. Radiative and 3-Body Recombination in Alcator C-Mod. *Submitted to Phys. of Plasmas*, October 1996.
- [27] P.C. Stangeby and G.M. McCracken. Plasma Boundary Phenomena in Tokamaks. *Nuclear Fusion*, 30(7):1323, 1990.
- [28] I.H. Hutchinson. Personal Communication, 1997.